A study on preparation of liquid crystalline single-walled carbon nanotube aqueous dispersions and their liquid crystal phase behaviors

Keiko Kojima

February 2023

A study on preparation of liquid crystalline single-walled carbon nanotube aqueous dispersions and their liquid crystal phase behaviors

Keiko Kojima

Doctoral Program in Chemistry

Submitted to the Degree Programs in Pure and Applied Sciences

of the Graduate School of Science and Technology in Partial Fulfillment

of the Requirements for the Degree of Doctor of Philosophy in

Science

at the

University of Tsukuba

Table of contents

Chapter 1　General introduction

1.1　Carbon nanotubes and their applications
1.1.1　Single-walled caron nanotubes (SWCNTs)

Carbon is the most familiar element and is contained in various kinds of chemical compounds. Because of hybrid orbitals of carbon atoms, such as sp, sp^2, sp^3 hybridizations, single, double, and triple bonds are formed in carbon-carbon bonds. Carbon allotropes with different chemical structures are well known (Table 1.1). Especially, the research on fullerene and graphene were awarded the Nobel Prize in chemistry (1996) and physics (2010). Therefore, carbon nanotube has also been attracted great interest.

Table 1.1 List of carbon allotropes classified by the forms of the carbon-carbon bond.

Hybrid orbital (Carbon-carbon bond)	sp hybridization (Triple bond)	sp^2 hybridization (Double bond)	sp^3 hybridization (Single bond)
Allotrope	Carbyne	Fullerene Carbon nanotube Graphene Graphite	Diamond

Single-walled carbon nanotubes (SWCNTs) which are discovered by S. Iijima in 1993[1] are nanoscale carbon allotrope made by rolling up a single graphene sheet (Fig. 1.1). Lengths of SWCNTs are more than 1000 times larger than the diameters, therefore, they have fiber-like structures with flexibility. Since SWCNTs consist of sp^2 carbons, they are highly stable materials and have high tensile strength[2-4]. They also have high mechanical strength and outstanding electronic properties which are derived from the properties of graphene sheets.

To apply superior properties to materials, SWCNTs have been widely used. For example, they are applied as fillers of electrodes of Li-ion battery and O-ring to add SWCNT's properties to materials[5,6]. Especially, because of their fiber-like structures, SWCNTs are highly expected to form fibers with high mechanical strength and electrical conductivity.
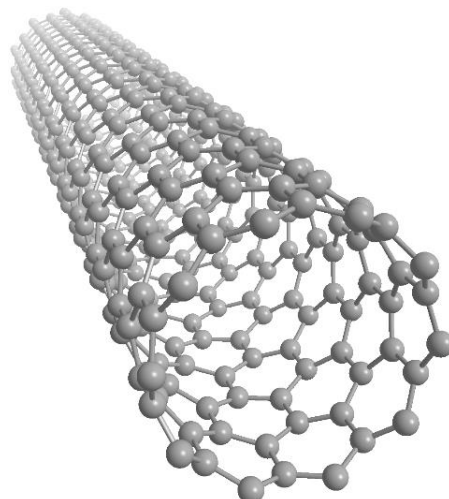
Figure 1.1 Molecular model of single-walled carbon nanotube.

1.1.2 Relationship between orientation of SWCNT in materials and material property

Because SWCNTs have a high aspect ratio, their superior properties always appear along the tube direction. Thereby the property of SWCNT material is affected by the orientation of SWCNTs in the material. Figure 1.2 shows the results of the resistance measurement of the ordered-SWCNT film[7]. The resistance value of the SWCNT film in which SWCNTs were lined up parallelly between electrodes was lower than the film in which SWCNTs were lined up perpendicularly. This is because the electrical resistance increases as increasing the number of SWCNT junctions. Further, SWCNT fibers with different order parameters expressed different electrical conductivities. Figure 1.3 shows scanning electrical microscope (SEM) images of the surface of SWCNT fibers[8]. The SWCNT fiber with higher electrical conductivity was formed from SWCNTs which are highly ordered (Fig. 1.3 (a)). Therefore, controlling SWCNT orientations is much important in the manufacture of high-performance SWCNT materials.
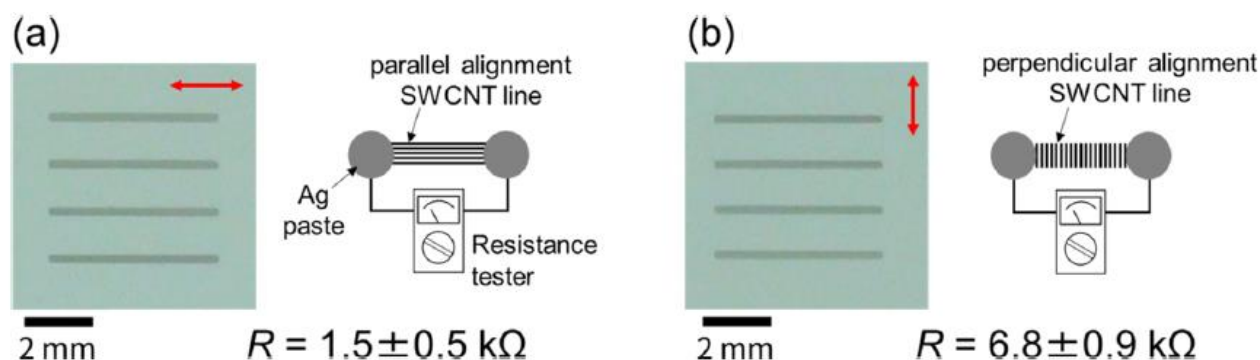
Figure 1.2 The resistance measurements of ordered-SWCNT films in which SWCNTs were lined up (a) parallelly or (b) perpendicularly between electrodes[7]. (Reprinted with permission from H. Jintoku *et al.*, *ACS Appl. Nano Mater.* **2022**, *5*, 2, 2195-2203. Copyright 2022 American Chemical Society.)
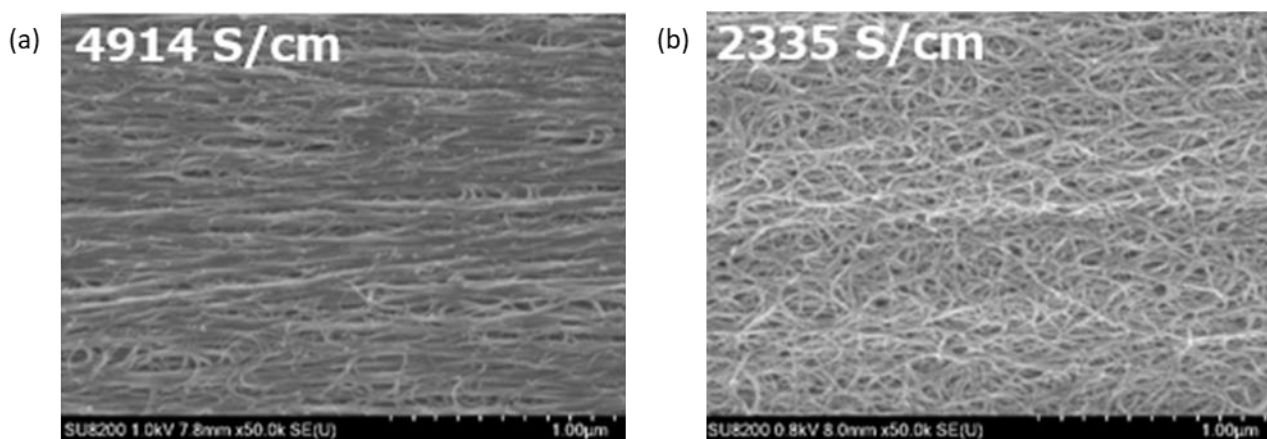
Figure 1.3 SEM images of the surface of SWCNT fibers. The electrical conductivities of each sample were (a) 4914 S/cm and (b) 2335 S/cm [8]. (Reprinted with permission from N. Tajima *et al.*, *Carbon* **2019**, *152*, 1-6. Copyright 2019 Elsevier.)

1.1.3　Controlling of CNT orientation in a macroscopic structure

  Methods of controlling CNT orientations are divided into two groups, dry process and wet process[9,10]. One of the examples of the dry process uses CNTs growing on a substrate like forests. Aligned CNT materials are prepared by directly withdrawing from the edge of the forest or picking out the part of vertically growing CNTs (Fig. 1.4 (a, b))[11,12]. Aligned CNT fibers can also be produced by withdrawing CNTs in the gas phase which are synthesized by the chemical vapor deposition (CVD) method (Fig. 1.4 (c))[13]. On the other hand, in the wet process, CNT materials are made from liquid crystalline SWCNT dispersions (Fig.1.4 (d)). The CNT orientation in the liquid phase prompts highly ordered SWCNTs[14,15]. Figure 1.5 shows the plot of the electrical conductivity against the Herman orientation factor of commercially available CNT fibers[9]. Dexmat CNT fibers made by the wet process and Nanocomp CNT fibers made by the dry process had similar orientation factors and high electrical conductivities. Therefore, both processes are suitable for manufacturing highly ordered CNT materials.

  However, the CNT synthesis methods adaptable for the dry processes are limited and the improvement of the CNT properties is basically difficult. For example, the array forming by directly withdrawing from the edge of the forest can be fabricated only from multi-walled CNT, at present. By contrast, the wet process can be applied to CNTs by any synthesis method. In addition, large-scale production of CNT materials is expected for the wet process by using existing printing processes such as roll to roll coating. Therefore, the wet process with liquid crystalline SWCNT dispersions is the effective and versatile process to control SWCNT orientation in macroscopic structures.
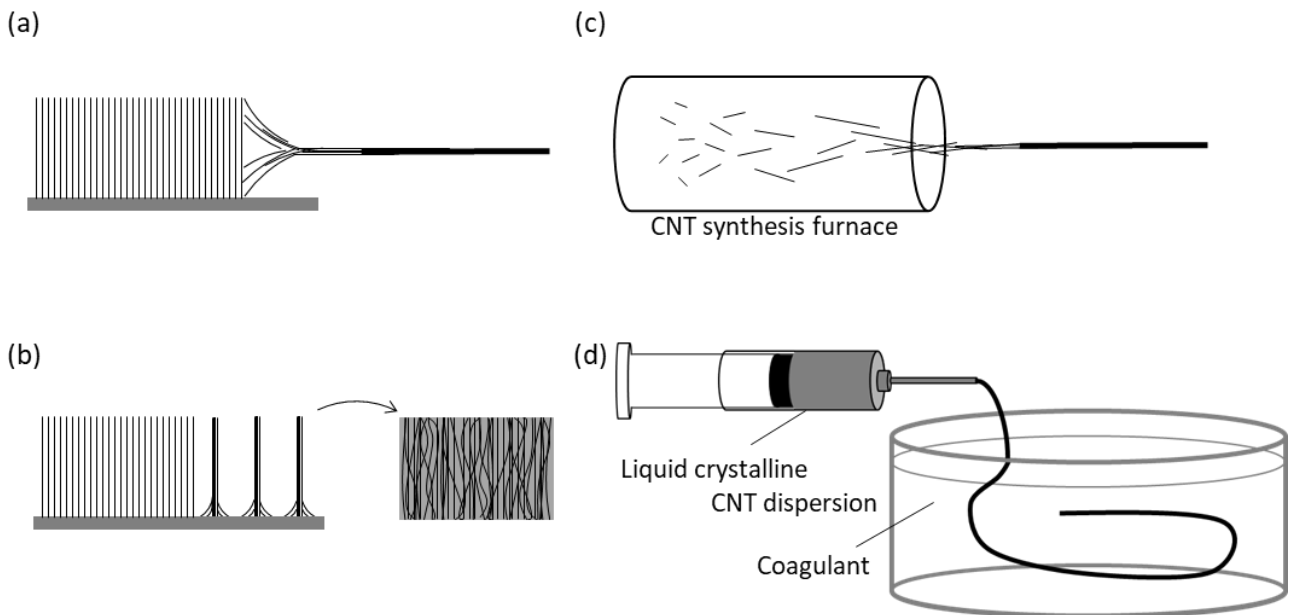
Figure 1.4 (a) Array forming process by directly withdrawing from the edge of the forest. (b) Array forming process by picking out the part of vertically growing CNTs. (c) Direct forming process. (d) Schematic of wet process.
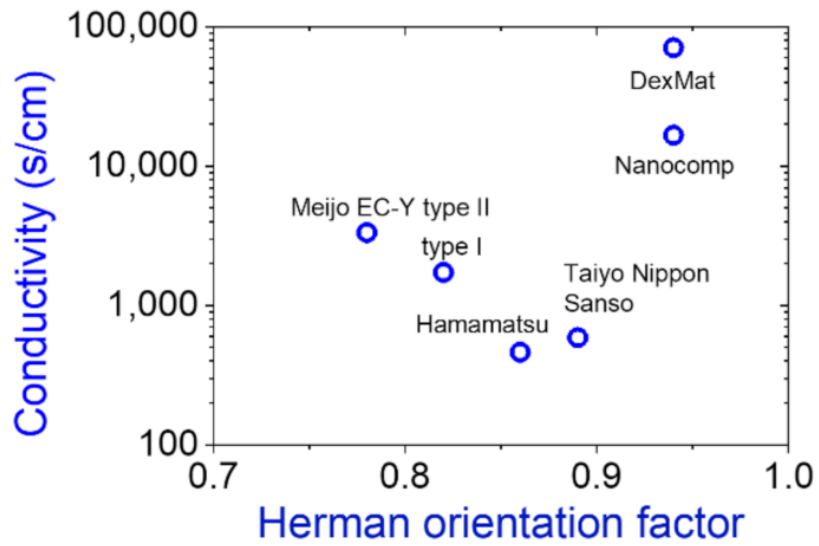
Figure 1.5 The plot of the electrical conductivity against the Herman orientation factor of commercially available CNT fibers[9]. (Reprinted with permission from T. Watanabe *et al.*, *Nanomaterials* **2022**, *12*, 539. Copyright 2022 Multidisciplinary Digital Publishing Institute.)

1.2 Liquid crystalline SWCNT dispersion

1.2.1 Preparation of liquid crystalline SWCNT dispersions

Liquid crystalline SWCNT dispersions can be prepared by concentrating well-dispersed SWCNT solutions[15-30]. SWCNTs need to be dissolved individually or bundled in solvents to form the liquid crystal (LC) phase and these rod-like SWCNTs act as mesogens. However, SWCNTs are strongly aggregated by the tube-tube van der Waals interaction between SWCNT surfaces. Therefore, it is necessary to untangle and stabilize them as individual or bundle forms in the dispersions.

In general, SWCNTs are dispersed by chemical or physical modification of SWCNT surface. In the chemical modification process, SWCNT walls are modified or protonated by superacid[15-17,19,21,29,30]. It has been known that SWCNT dispersions treated with chlorosulfonic acid (CSA, a superacid) show the LC phase[15-17,21,29,30]. In CSA, SWCNT acts as a weak base that can be protonated. The protonation induces a Coulomb repulsion between SWCNTs, which overcomes the strong tube-tube van der Waals interaction[17]. Thereby, the individual SWCNTs are thermodynamically stable in the CSA dispersion. In fact, this process has produced highly ordered CNT fibers and films[14-16,21,29,30]. Even though CSA is considered to be the best solvent for dispersing SWCNTs, special care such as ventilated facilities, proper treatment of the waste solvents, and the protection of the equipment is required in the dispersion process. Therefore, a safer method is highly desired for further applications.

On the other hand, in the physical modification process, dispersants adsorb on SWCNT walls. A popular way to disperse SWCNTs is to mix them with dispersants and sonicate them in water[18,20,22-28]. For instance, the LC phase transitions have been successfully observed in DNA-assisted SWCNTs aqueous dispersions[18,25,26]. The nematic LC phase has been observed via polarized optical microscopy with a SWCNT concentration above 4 wt%[16]. Zhang *et al.* reported the LC phase of sodium dodecylbenzene sulfonate (SDBS)-assisted SWCNTs in water[23]. By evaporating a droplet of a SDBS-assisted SWCNT dispersion, the isotropic-to-nematic transition occurs from the edge of the drying droplet. Puech *et al.* investigated the LC ordering of bile salt-stabilized SWCNTs[24]. They prepared SWCNTs with different tube lengths by controlling the sonication process. Short SWCNTs tend to form highly ordered LCs. Although there have been several reports on dispersant stabilized SWCNT LCs, a systematic examination and detailed characterization of the isotropic-to-biphasic-to-nematic phase transition, which encompasses the phase transition behaviors of SWCNTs, the shape of the LC droplets in the biphasic state, and the texture and disclination in the nematic phase, are limited.

1.2.2 Transition of SWCNT dispersion states during dispersion process

SWCNTs exist in powder form and are strongly aggregated by the tube-tube van der Waals interaction between SWCNT surfaces (Fig. 1.6 (a)). Therefore, SWCNTs are dispersed gradually in dispersing steps as in Figure 1.6 (b). First, SWCNT powder was defibrated and large agglomerates in the size of μm – mm were formed. In the further dispersing step, the agglomerates were dispersed and changed into isolated SWCNT or SWCNT bundles consisting of a few SWCNTs. Thus, dispersions of SWCNT normally contain SWCNT particles with a wide range of sizes. Because large agglomerates and small rod-like SWCNTs are coexisting in dispersions, general particle size analysis methods such as dynamic light scattering (DLS) and laser diffraction (LD) analysis are not suitable for quantitatively

analyzing the SWCNT dispersion states. In our previous research, it is confirmed that differential centrifugal sedimentation (DCS) analysis can estimate particles from a dozen μm to several nm in size[8,31].
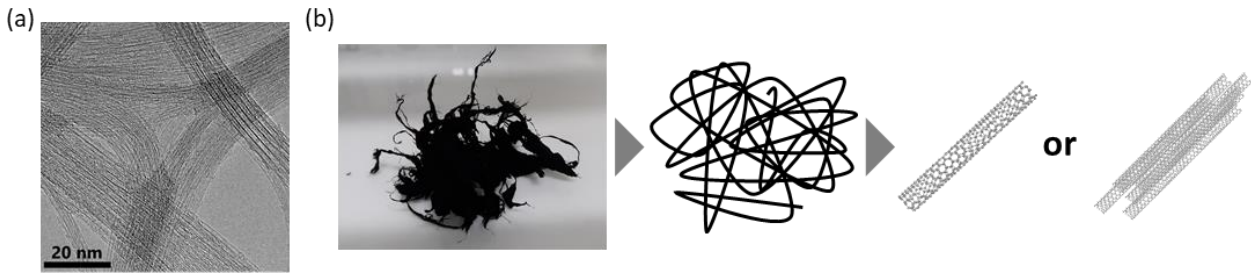

Figure 1.6 (a) Transmittance electron microscope image of SWCNT powder. (b) Schematic of SWCNT dispersion process. SWCNT powder (left) become agglomerates (middle) in the size of μm – mm and/or isolated SWCNT or SWCNT bundle (right) during the dispersion process.

1.2.3 Differential centrifugal sedimentation (DCS) analysis

DCS analysis is the technique that combines size classification by sedimentation process of density gradient centrifugation and detection of particles by transmittance measurement. Figure 1.7 (a) shows a schematic illustration of density gradient centrifugation. First, a sample is layered on top of a density gradient media. Particles in dispersion are settling at a constant velocity by centrifugal force. This is called terminal velocity determined by the balance between the viscous resistance and the centrifugal force (Fig. 1.7 (b)). According to Stokes' law, the settling velocity is calculated by

$$v = D^2 \frac{(\rho_{SWCNT} - \rho_0)R\omega^2}{18\eta} \qquad \text{(Eq. 1.1)}$$

where D is the diameter of the settling particle, ρ_{SWCNT} is the density of SWCNT (In this thesis, 1.5 g/cm^3 is used as ρ_{SWCNT}.), ρ_0 is the average density of the gradient media, R is the distance between the center of centrifugation and the position of the settling particle, ω is the rotational velocity, and η is the average viscosity of the gradient media. This equation indicates that the settling velocity is proportional to the square of particle diameter D, which is called Stokes diameter D_{Stokes}. It can be calculated from Eq 1.1,

$$D_{Stokes} = \sqrt{\frac{18\eta \ln\frac{R_f}{R_0}}{(\rho_{SWCNT} - \rho_0)\omega^2 t}} \qquad \text{(Eq. 1.2)}$$

where R_0 and R_f are the distances from the center of centrifugation to the liquid surface of density gradient media and the position where the particle is detected, and t is the required time from the start of particle settling till particle detection. From Eq. 1.2, the Stokes diameter D_{Stokes} can be determined by t. On the other hand, in Stokes' law, the shape of the particle is assumed to be a spherical form. The Stokes diameter D_{Stokes} of a rod-like substance like SWCNTs is approximately expressed by

$$D_{Stokes} = d\sqrt{ln\left(\frac{2l}{d}\right)} \qquad \text{(Eq. 1.3)}$$

where d and l are the diameter and the length of the rod-like particle, respectively[31,32]. If a rod-like particle with d = 5 nm and l = 2 μm is measured by DCS analysis, D_{Stokes} is calculated to be ~13 nm by Eq. 1.3. Therefore, rod-like SWCNTs are detected at a slightly larger size than the actual diameter in DCS analysis.

(a)   (b)

| Viscous drag | $3\pi D\eta v$ |

| Centrifugal force | $(\rho_{CNT} - \rho_0)VR\omega^2$ |
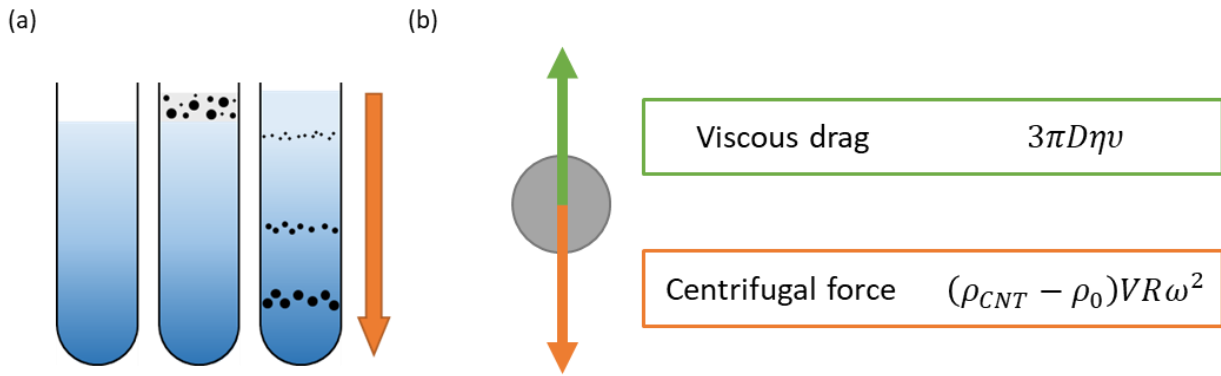
Figure 1.7 (a) Schematic of density gradient centrifugation. Orange arrow indicates the direction of settling. (b) Forces around the particle.

1.3   General objective

The objectives of this thesis are to establish a preparation method for liquid crystalline surfactant-stabilized SWCNT aqueous dispersions and to examine their LC phase behaviors. Chapter 2 discusses the results of the optimization of dispersing process to prepare rod-like SWCNT by DCS analysis and the relationship between SWCNT size and LC phase behaviors. Additionally, in Chapter 3, the effect of dispersant species on phase transition behavior is estimated by comparing rod-like SWCNT dispersions with different surfactants. Also, the SWCNT orientations in LC phases are observed in detail (Chapter 4).

This thesis is expected to become a guideline for the efficient preparation method of liquid crystalline surfactant-stabilized SWCNT aqueous dispersions for the wet process of highly oriented SWCNT materials.

Chapter 2   Liquid crystalline behaviors of SWCNT-SC dispersions with different SWCNT size

2.1   Introduction

There have been several reports on dispersant-stabilized liquid crystalline SWCNT dispersions, but the liquid crystalline behaviors, such as phase transition concentrations and LC phases, of these reports can't be compared because the SWCNT dispersion states were not quantitatively estimated. Therefore, to estimate the effect of SWCNT sizes on phase behaviors, the SWCNT dispersion states in dispersions should be examined by quantitative method.

In this chapter, SWCNT aqueous dispersions displaying LC phases with the aid of sodium cholate were prepared. Because sodium cholate, known as a good dispersant for SWCNTs, is a salt of cholic acid, which is a primary bile acid, it is biocompatible and environmentally friendly. To optimize the dispersion conditions, SWCNT dispersion states were examined by optical microscopy and DCS analysis. Furthermore, comparing two dispersions made by the optimized dispersion process, the relationship between SWCNT size and LC phase behaviors is discussed.

2.2 Experimental section

2.2.1 Optimization of dispersion process to obtain rod-like SWCNTs

SWCNTs were purchased from Meijo Nanocarbon (eDIPS EC-DX, Lot. 5R79I25C). SWCNT powder was defibrated by stirring in a viscous solvent[33]. At first, 100 mg of SWCNT powder and 100 mL of glycerol (Wako) were stirred for 18 hours at 500 rpm (AS ONE, HPS-100PD). Afterward, the excess glycerol was removed by mixing the SWCNT-glycerol mixture with 200 mL of water and subsequent vacuum filtration (Merck, Omnipore^{TM} 1.0 μm PTFE membrane). To completely remove glycerol from SWCNTs, the water and filtration process was repeated until 2 L of water passed through a filter and a SWCNT wet cake was obtained. The cake was redispersed in 50 mL of 10 mg/mL sodium cholate (SC) (Wako) aqueous solution. To optimize the dispersion method, three dispersing methods, mill mixer (OSAKA CHEMICAL Co., Ltd., Force Mill), bath sonicator (Cosmo Bio Co., Ltd., Bioruptor UCD-250), and probe sonicator (Sonics, VCX500) equipped with a titanium alloy tip (TI-6AL-4V) were tried. In the mill mixer process, 50 mL of the SWCNT-SC mixture was treated by shear stress for 25 minutes (On/Off = 30 s/2 min). In the bath sonicator process, 15 mL of the mixture was divided into three and sonicated for 12 hours (Output: 250 W, On/Off = 30 s/10 s) in the water bath at 15°C. In the probe sonicator process, 10 mL of the mixture was sonicated for 10 – 20 minutes (Output: 30%, On/Off = 1 s/1 s) in the water bath at 15°C.

2.2.2 Estimation of SWCNT dispersion states

The prepared dispersions were observed under an optical microscope (OLYMPUS, DSX510) to confirm the dispersion state of SWCNTs. Furthermore, a DCS analyzer (CPS Instruments Inc., CPS 24000 UHR (CR-39)) was used to measure the size distribution of the SWCNT bundles[31]. Figure 2.1 shows an overview of the DCS analyzer. During the measurement, the disc cell rotated at 22,000 rpm. The density gradient was created by sucrose, which concentration was 8 wt% - 24 wt%. The SWCNT dispersions were injected into the center of the cell and reached the top of the density gradient media. The analyzer collected the data of absorption intensities against the settling time t. Because of the variability of the density gradient, the correlation between the Stokes diameter D_{Stokes} and t (Eq. 1.2) is not always consistent. Therefore, the calibration measurement of the standard sample was conducted in each measurement.
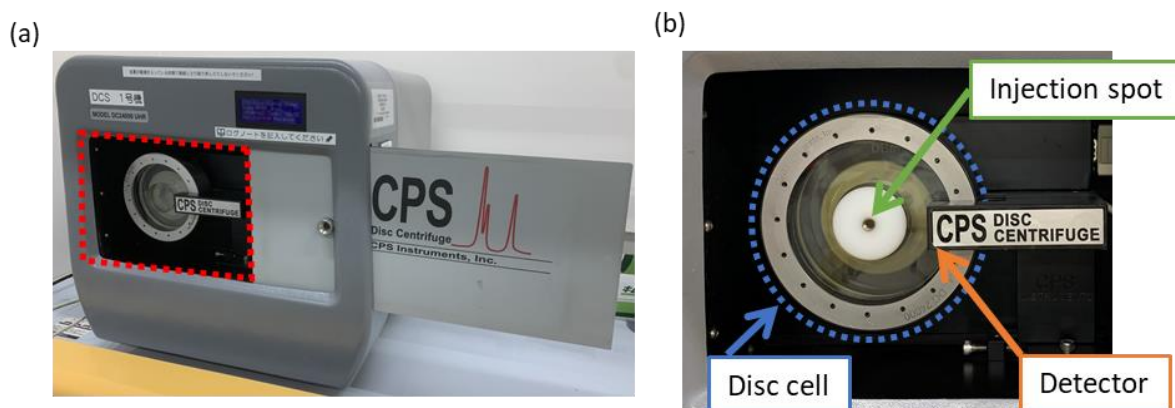

Figure 2.1 (a) An overview of disc cell in DCS analyzer (CPS Instruments Inc., DC24000 UHR). (b) An enlarged view of the area surrounded by a red dotted line in Fig. 2.1 (a).

2.2.3　Comparison of SWCNT species

Dispersions of other species of SWCNT were also prepared by a probe-type sonicator. Tuball[TM] (OCSiAl, high purity product), ZEONANO® (Sigma Aldrich), CoMoCAT[TM] (Sigma Aldrich, CG300), and APJ-SSA (Meijo Nanocarbon) were used. A mixture of 20 mg of each SWCNT powder and 10 mL of 10 mg/mL SC aqueous solution was sonicated by a probe-type sonicator for 40 minutes. The solution was centrifuged with a centrifuge (KOKUSAN, H-36) at 4000 g for 30 minutes to remove large SWCNT agglomerates and impurities. Then, each solution was observed by a scanning electron microscope (SEM) and measured by a DCS analyzer (CPS Instruments, CPS 24000 UHR (CR-39)).

2.2.4　Preparation of liquid crystalline SWCNT-SC dispersions

SWCNT powder of eDIPS was dispersed by a two-step process which consists of defibration by stirring in glycerol and dispersion by probe sonicator in SC aqueous dispersion (See section 2.2.1). The dispersions were sonicated for 40 – 60 minutes until all agglomerates were smaller than 100 μm under the observation of the optical microscope and centrifuged with a centrifuge (KOKUSAN, H-36) at 4000 g for 30 minutes to remove large SWCNT agglomerates and impurities. To concentrate the dispersion, it was ultrafiltrated (MILLIPORE, Amicon® Ultra-4, MWCO = 100,000) at 1000 g for 5 minutes (KOKUSAN, H-36) and stirred by pipetting to avoid SWCNT reaggregation. The SWCNT concentrations were calculated from the optical absorption intensity at 735 nm measured by a spectrometer (Shimadzu, UV-3100). To estimate the concentration of SWCNTs in the dispersion, the calibration curve (Fig. 2.2) was prepared by the following process. A homogenized SWCNT dispersion was prepared by using an SWCNT sample whose weight was measured, and then six diluted SWCNT dispersions were prepared by using the dispersion. In the near-infrared region, only SWCNT has optical absorption. Therefore, the concentration dependence of the absorbance at 735 nm was used as a calibration curve. An approximate line (dashed line in Fig. 2.2) is expressed by

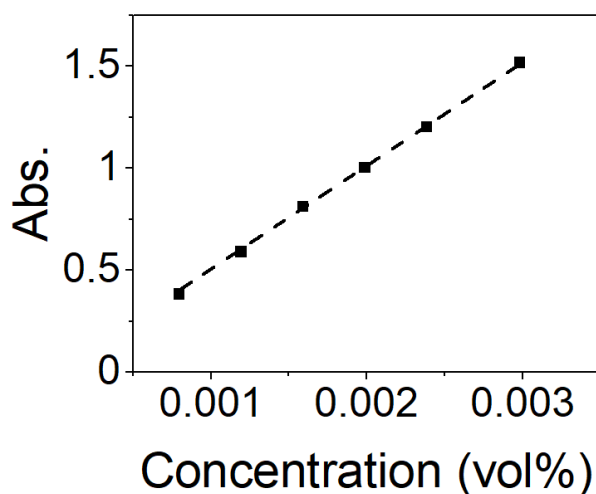$$y = 33.73x \hspace{3cm} \text{(Eq. 2.1)}$$

Figure 2.2 Calibration curve of SWCNT-SC dispersion. Vertical axis indicated the absorption intensity at 735 nm. (Reprinted with permission from K. Kojima *et al.*, *Applied Physics Express* **2022**, *15*, 125003. Copyright 2022 The Japan Society of Applied Physics)

2.2.5 Size measurement of rod-like SWCNTs

The shapes of SWCNTs in the dispersion were estimated by a scanning electron microscope (SEM) and an atomic force microscope (AFM). The specimen was prepared by dip-coating on the Si substrate (2 cm^2), which was washed with acetone and irradiated with UV light (Meiwafosis, PC-450 plus) for 15 minutes before the process. Next, the substrate was dipped into the diluted solution (a mixture of 20 μL SWCNT dispersion and 20 mL of water). Finally, the substrate was slowly extracted and maintained vertically until dry. Furthermore, the average diameter of a single SWCNT in eDIPS powder was measured by a transmittance electron microscope (TEM).

2.2.6 Observations of LC phases

The concentration of dispersions was adjusted by adding a 10 mg/mL sodium cholate solution. The solutions were encapsulated in a glass capillary (VITROCOM, VitroTubes^{TM} 5012-050, cavity size: 0.1 mm × 2 mm × 50 mm) by UV resin. The encapsulated solutions sat for one week to reach equilibrium. The LC phases were observed by a polarized optical microscope (POM) (OLYMPUS, DSX510) under crossed Nicols.

Figure 2.3 (a) shows the configuration of POM. There are two polarizers above and below the sample stage, and they are called polarizer (lower one) and analyzer (upper one). When the direction of the polarization axis of the polarizer is orthogonal to that of the analyzer, they are in the position in the crossed Nicols. If the aligned specimen is rotated 360° under crossed Nicols, it sequentially changes bright and darker in each 45°. As shown in Fig. 2.3 (c), when the alignment direction of the specimen is oriented at 45° angle to the axis of the polarizer, the specimen looks brightest.

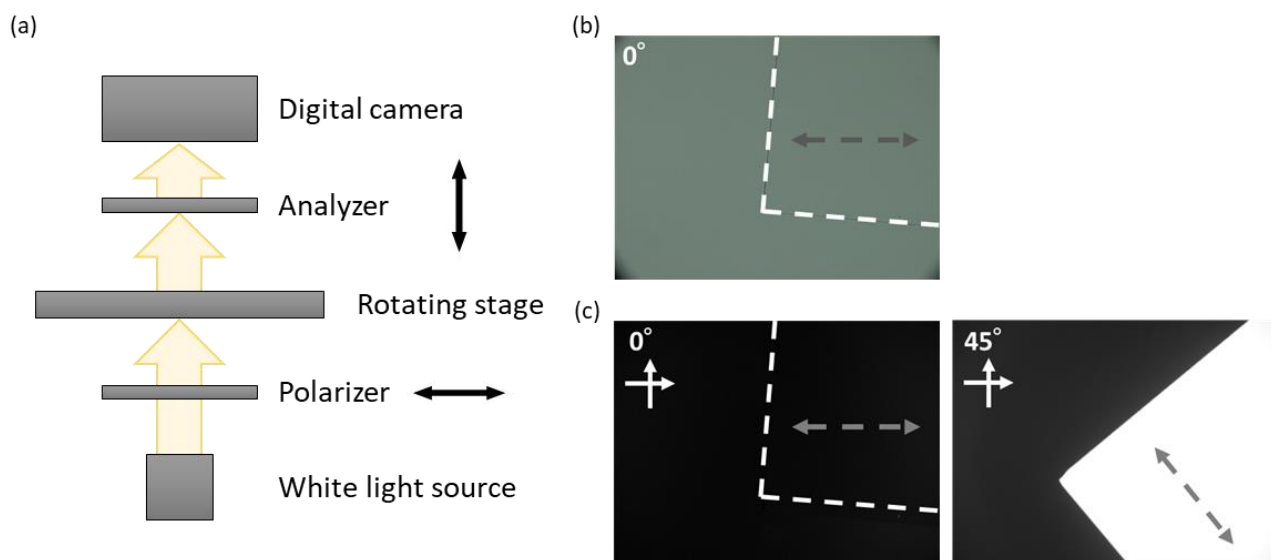Figure 2.3 (a) The configuration of POM. (b) An optical microscope image of a standard aligned sample. It is placed in the area enclosed by the white dashed line. Gray dashed line indicates the orientation direction of the sample. (c) POM images of a standard aligned sample were observed at 0°and 45°. The sample was placed in the same position as Fig. 2.3 (b). White arrows indicate the direction of the polarizer and the analyzer.

2.2.7 Preparation of the aligned SWCNT films

Figure 2.4 shows a schematic of the method of film preparation by the simple bar coating method. The specimen was prepared on the glass slide, which was washed and irradiated with UV light (Meiwafosis, PC-450 plus) for 60 minutes before the process. A droplet of 20 μL of the liquid crystalline SWCNT dispersion was dripped on the glass slide and coated by bar coater (OSG SYSTEM PRODUCTS Co., LTD, Select-Roller L60, OSP-10 (Bar groove pitch: 0.2 mm, depth: 24 μm)) at 5.5 cm/s. Then, the specimen was left until the SWCNT film was completely dried. To estimate the SWCNT orientation, the films were observed by POM observation and measured by polarized optical absorption spectroscopy. Further, the aligned films were characterized by optical absorption spectroscopy (Jasco, V-770).
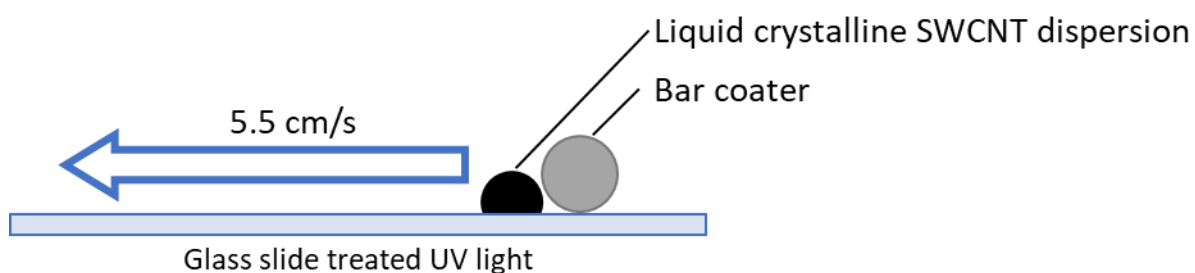

Figure 2.4 A schematic of the method of film preparation by the simple bar coating method.

2.3   Results and discussion

2.3.1   Optimization of dispersion conditions

To select the optimal dispersion method, SWCNT-SC dispersions were prepared by three methods: mill mixer, bath sonicator, and probe sonicator. Figure 2.5 (a-c) show optical microscope images of each dispersion. The dispersion prepared by the bath sonicator included the largest agglomerate and showed wide size ranges. In contrast, the agglomerates of the others were relatively uniform in size. To estimate the size distributions of SWCNTs, the dispersions were measured by DCS analysis. Figure 2.5 (e) shows the results of DCS analysis, where the horizontal and vertical axes denote the Stokes diameter and the absorption intensity, respectively. If the Stokes diameter of SWCNTs is larger than 0.1 μm, it is expected that SWCNTs form a mesh-like agglomerate[31]. By contrast, if the Stokes diameter of SWCNTs is smaller than 0.1 μm, it is expected that SWCNTs form a rod-like shape. Based on these, the dispersions prepared by the mill mixer and bath sonicator contained agglomerates as main components (Blue and green line of Fig. 2.5 (e)). On the other hand, in the dispersion prepared by the probe sonicator, the Stokes diameter of most SWCNTs was under 0.1 μm. This means that the SWCNTs or SWCNT bundles were individually dispersed in the dispersion.

The dispersion conditions were determined to prepare the dispersion without agglomerates. Based on the optical microscope image (Figure 2.5 (d)), almost no agglomerate was observed for the dispersion which was sonicated for a longer time. Additionally, the size distribution denoted red line in Fig. 2.5 (e) confirmed that rod-like SWCNTs were the main component. Thus, we selected the probe sonicator to obtain the dispersion of rod-like SWCNTs in this study.
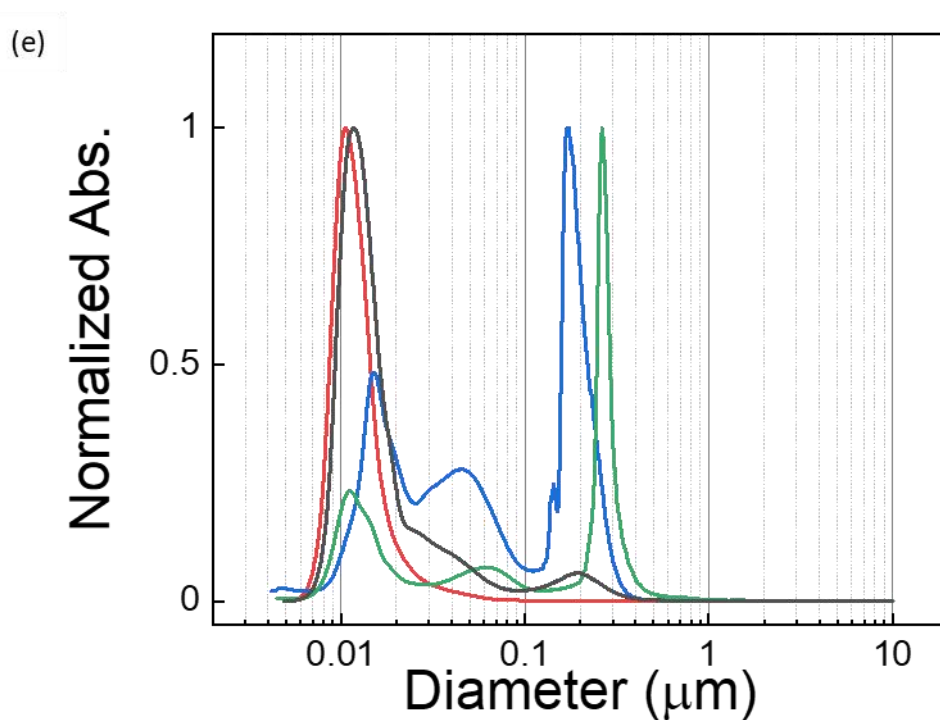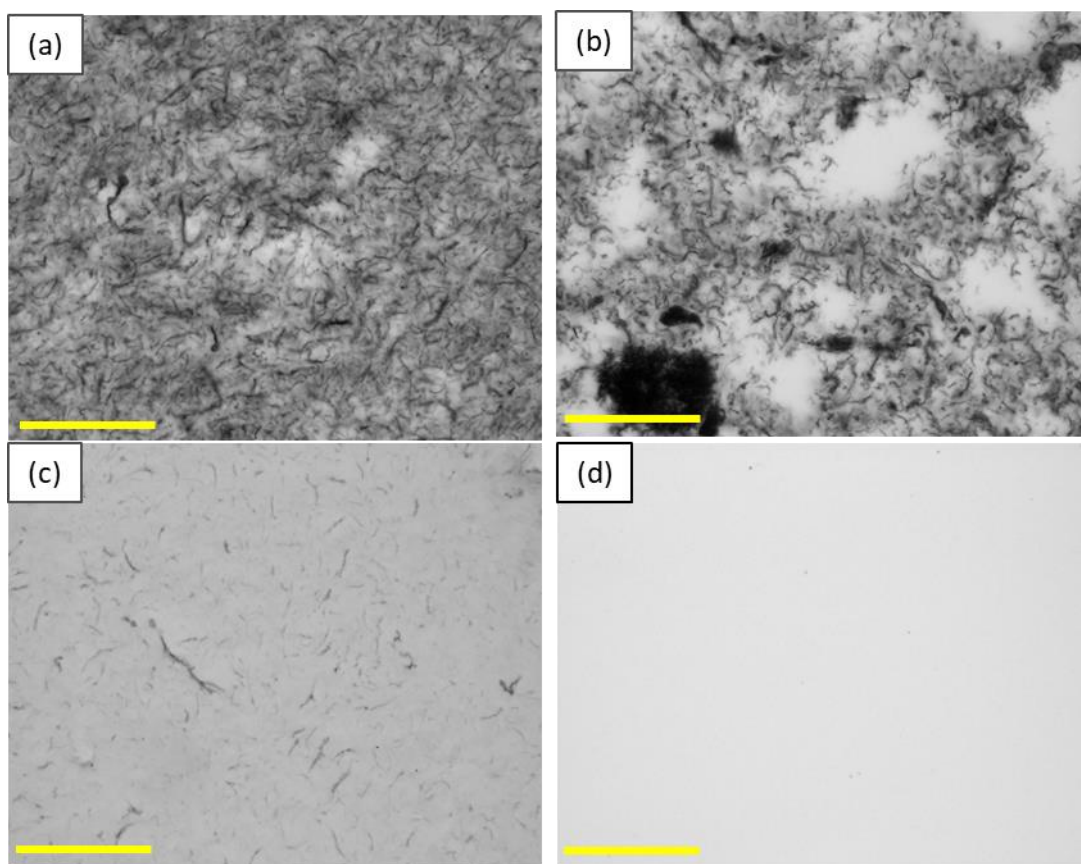
Figure 2.5 Typical optical microscope images of SWCNT-SC dispersions dispersed by (a) mill mixer, (b) bath sonicator, (c) probe sonicator, and (d) probe sonicator with the optimal sonication time. Scale bars are 100 μm. (e) The SWCNT size distributions of dispersions made by mill mixer (blue), bath sonicator (green), probe sonicator (black), and probe sonicator with optimal condition (red).

2.3.2 Comparison of SWCNT species

To obtain ideal rod-like SWCNTs for liquid crystalline SWCNT dispersion, several SWCNTs: eDIPS, Tuball, SG, CoMoCAT, and APJ-SSA were dispersed in the same process and compared. The general feature of each SWCNT was listed[34].

- eDIPS is synthesized by enhanced direct injection pyrolytic synthesis method[35]. The ratio of impurities, such as amorphous carbon and metal catalyst, is lower than other SWCNTs. Kinks and defects of SWCNT structure are few, therefore, eDIPS is known as the longest SWCNT with high crystallinity.

- Tuball is synthesized by CVD method. The purity is normally lower than eDIPS. There are few kinks and defects on the SWCNT wall. Therefore, Tuball is also known as long SWCNT with high crystallinity.

- SG is synthesized by super-growth method[36], which is a sort of the CVD method. SWCNTs grow on a catalyst substrate in the vertical direction. It is known that SG-SWCNTs normally show kinked structures.

- CoMoCAT is synthesized by CoMoCAT™ method which is a kind of the CVD method[37]. It is good at controlling SWCNT structures.

- APJ-SSA is synthesized by the arc discharge method, which is known as the large-scale synthesis method of fullerene. Generally, the powder contained a substantial amount of carbon impurities, and the purification process is needed before use. In this study, APJ-SSA-SWCNTs were purified by a methanol solution of sodium hydroxide[38].

Figure 2.6 (a) shows the SWCNT size distribution measured by DCS analysis in each dispersion. The intense peak at ~10 nm in the size distribution can be attributed to isolated SWCNTs or SWCNT bundles consisting of a few SWCNTs. Therefore, the dispersions of eDIPS, Tuball, and CoMoCAT were expected that they contained rod-like SWCNTs as a major component. On the other hand, because of the multimodal size distributions, it is confirmed that the dispersions of SG and APJ-SSA contained SWCNTs of various shapes. The actual shape of SWCNTs in each dispersion was evaluated by SEM observation (Fig. 2.6 (b-f)). Only eDIPS and Tuball contained SWCNTs with rigid rod shapes, and the others were composed of agglomerates bent at the atomic-scale defects in SWCNTs (SG and CoMoCAT) or the mixture of SWCNTs with large diameters (the Stokes diameter ~0.1 μm) and small diameter (the Stokes diameter ~0.01 μm) (APJ-SSA). From these results, it was revealed that eDIPS and Tuball were suitable SWCNT species to prepare rod-like SWCNTs. Furthermore, eDIPS and Tuball have been classified as the group in which SWCNT had high crystallinity[34]. Therefore, selecting SWCNT powder with high crystallinity seems to be an effective approach for the preparation of liquid crystalline SWCNT dispersion.
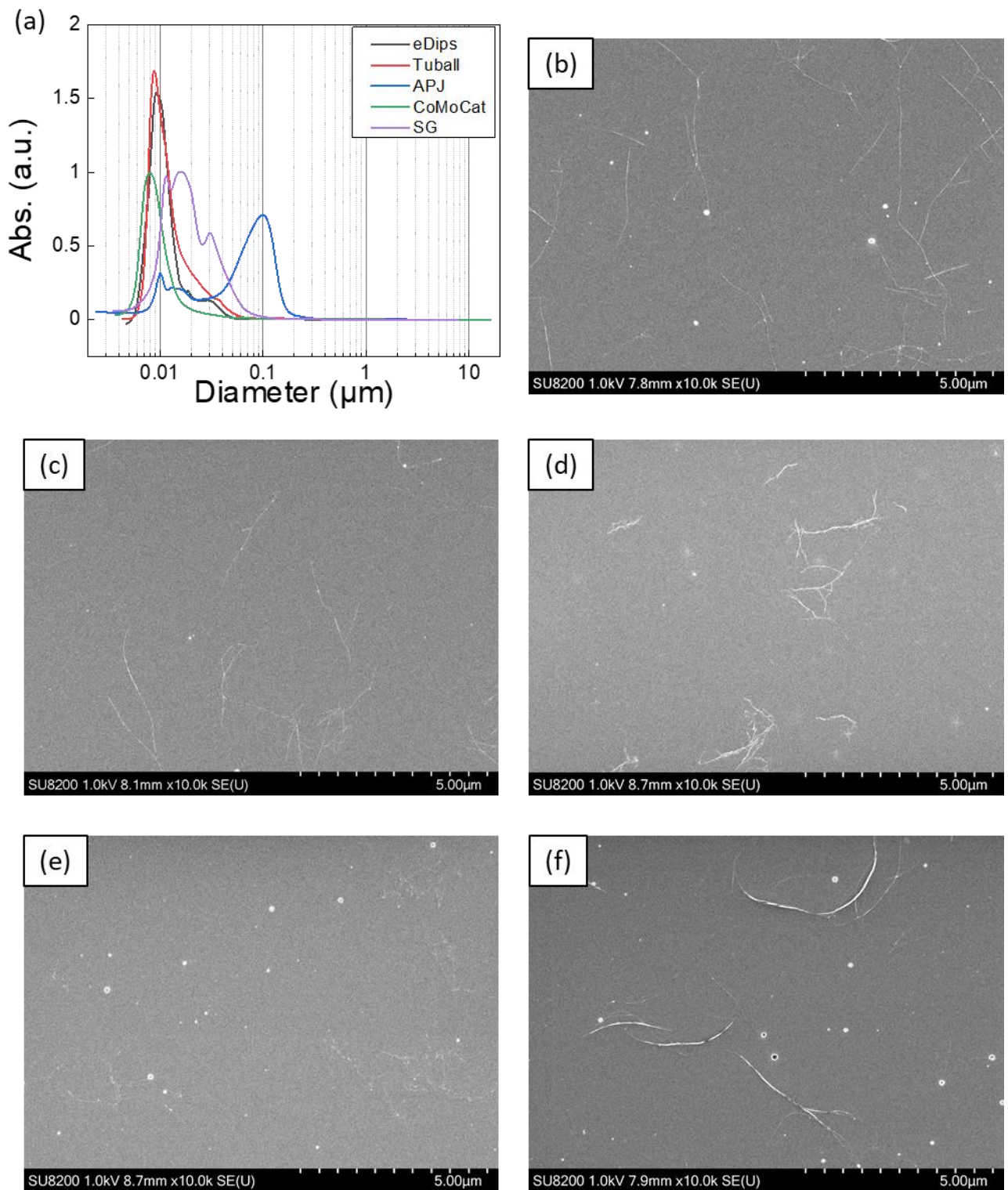
Figure 2.6 (a) The SWCNT size distributions of dispersions of eDIPS (black), Tuball (red), SG (purple), CoMoCAT (blue), and AJP-SSA (green). SEM images of SWCNTs in dispersions of (b) eDIPS, (c) Tuball, (d) SG, (e) CoMoCAT, and (f) APJ-SSA.
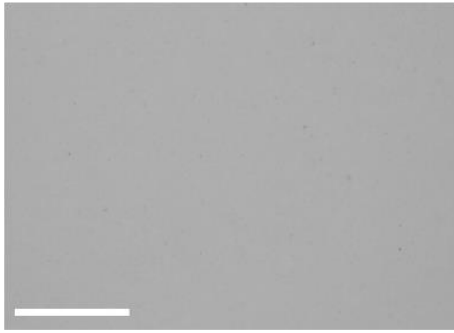
2.3.3 Estimation of SWCNT size in dispersions

To compare the phase transition behaviors of the SWCNT dispersions with different SWCNT sizes, two SWCNT-SC dispersions were prepared by the same procedures described in section 2.2.4 (they temporally stand for dispersion A and dispersion B). From the optical microscope images (Fig. 2.7 (a, h)), dispersion B contained some SWCNT agglomerates that were observed at around 0.4 µm in the DCS result (Fig. 2.7 (i), inset). The discrepancy between the actual size from the optical image (dozens µm) and the Stokes diameter (~0.4 µm) from DCS analysis can be attributed to the buoyancy caused by the difference in density between the density gradient media and the solvent[31]. Because the mesh-like agglomerates hold the solvent, the settling velocity becomes slower due to buoyancy. Therefore, the agglomerates were detected at a smaller (Stokes) diameter in DCS analysis than the apparent diameter. The intense single peaks at 9.2 nm and 11.6 nm were observed for both dispersion A and B, so it was expected that the dispersions mainly contained rod-like SWCNTs.
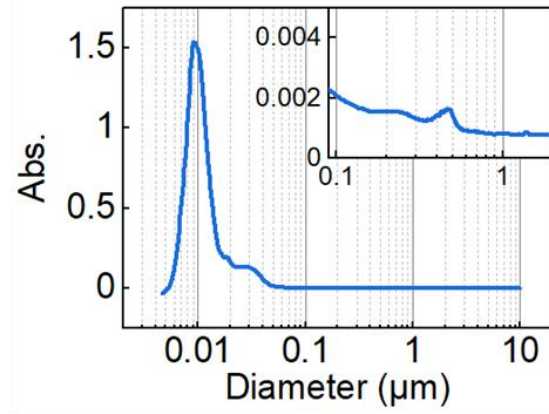
We obtained the distributions of SWCNT length (Fig. 2.7 (d, k)) based on the SEM observations (Fig. 2.7 (c, j)). We also conducted AFM observation (Fig. 2.7 (e, l)). Figure 2.7 (f, m) show the height profiles along the red lines in the AFM images (Fig. 2.7 (e, l), respectively). The distributions of SWCNT diameters estimated from the height profiles is shown in Figure 2.7 (g, n). Figure 2.7 (c) shows a typical SEM image of SWCNTs in dispersion A. Most SWCNTs had isolated forms, but a few agglomerates were more than 10 µm in size. The average SWCNT length L was ~1.9 µm. The AFM images showed that the height distribution ranged from 1 nm to 8 nm with an average diameter D of ~2.8 nm (Fig. 2.7 (g)). The SWCNT aspect ratio L/D of dispersion A is 665. On the other hand, the average length L and diameter D of SWCNTs in dispersion B were estimated to be ~1.7 µm and ~1.5 nm, resulting in $L/D = 1088$. (Hereafter, the dispersion A ($L/D = 665$) and B ($L/D = 1088$) stand for SC-low and SC-high.) From the TEM observation, the average diameter of single SWCNTs used here is 1.65 nm. From the distributions of the SWCNT diameter in the dispersions, both the isolated SWCNTs and the bundles of several SWCNTs were contained.

The Stokes diameters of rod-like particles were calculated to be 7.5 nm in SC-low and 4.2 nm in SC-high by Eq. 1.3. These values were comparable with the intense peaks of the DCS results (Fig. 2.7 (b, i)), indicating the present procedure produces a uniform dispersion of rod-like SWCNTs.

(a)

(b)

Abs.

1.5

1

0.5

0

0.004

0.002

0.1   1

0.01   0.1   1   10

Diameter (µm)

(c)

SU8200 1.0kV 7.8mm x10.0k SE(U)   5.00µm

(d)

Count

30

20

10

0

0   2   4   6   8   10   12

Length (µm)

(e)

3.33
[nm]

0.00

(f)

3.24
[nm]

2.70 nm

0.00

0.00   1.41 [µm]

(g)

Count

10

5

0   2   4   6   8   10

Diameter (nm)
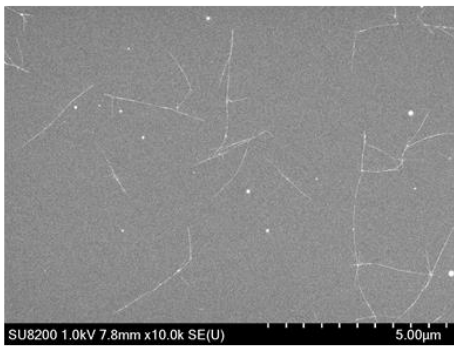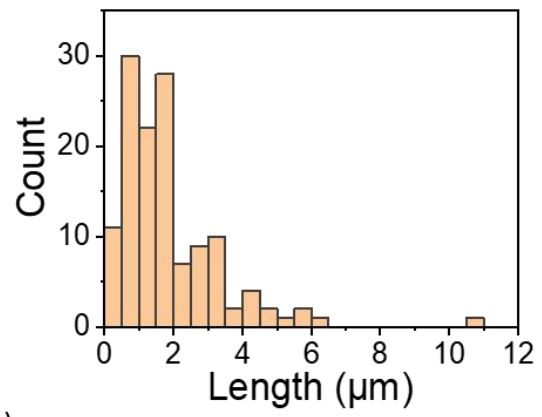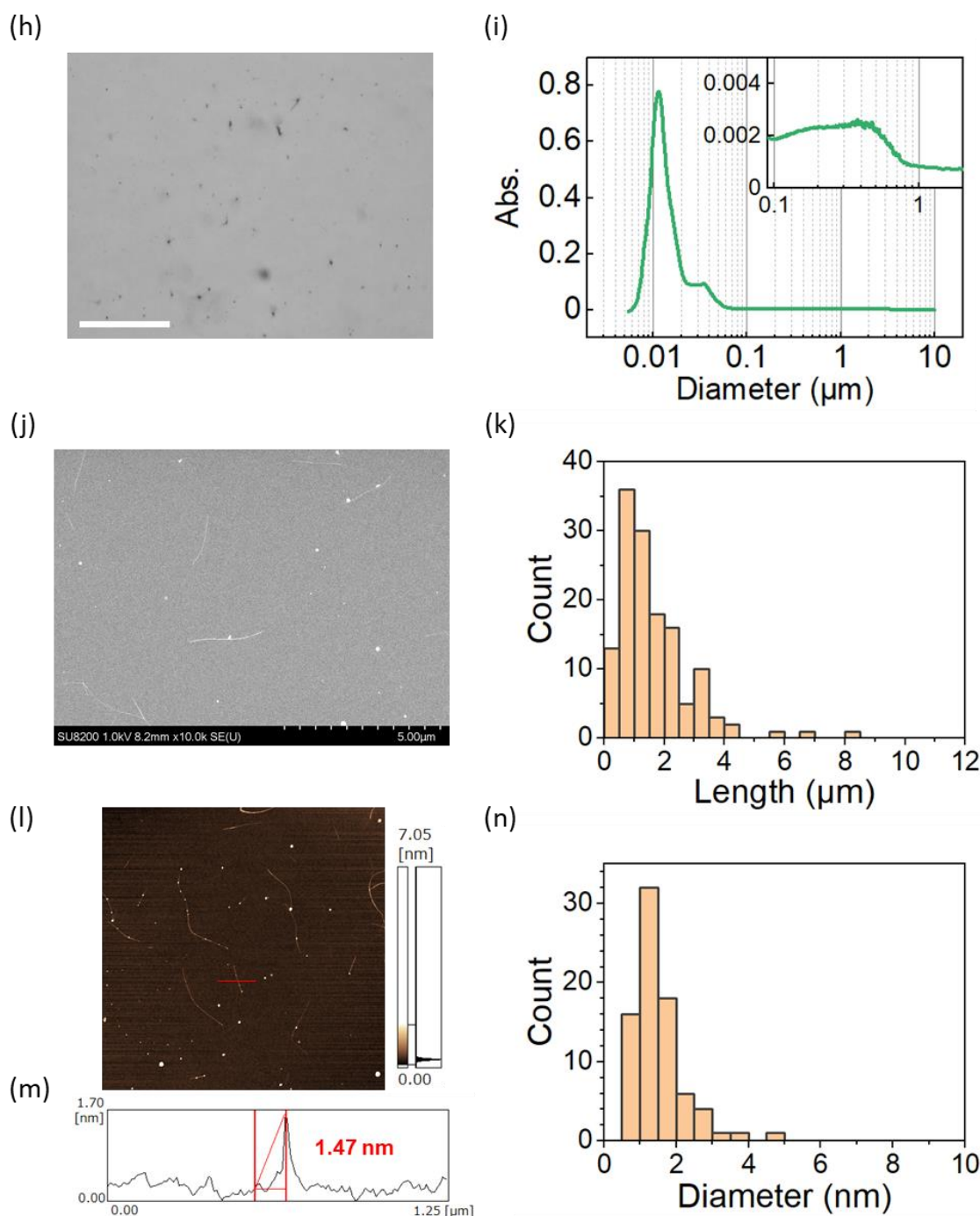
Figure 2.7 (a) A typical optical microscope image of SC-low. Scale bar is 100 μm. (b) The SWCNT size distribution of SC-low. (c) A typical SEM image. (d) Histogram of SWCNT length in SC-low from SEM. (e) A typical AFM image. The size of the image is 10 μm square. (f) AFM height profile at the red line in Fig. 2.7 (e). (g) Histogram of SWCNT diameter in SC-low from AFM. (h) A typical optical microscope image of SC-high. Scale bar is 100 μm. (i) The SWCNT size distribution in SC-high. (j) A typical SEM image. (k) Histogram of SWCNT length in SC-high from SEM. (l) A typi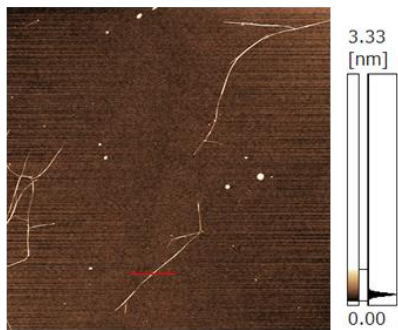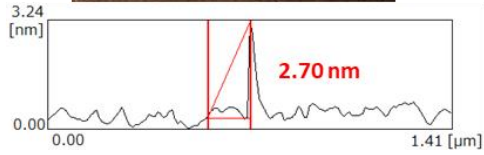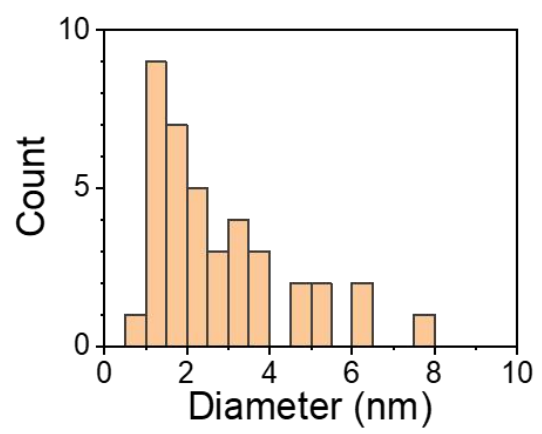cal AFM image. The size of the image is 10 μm square. (m) AFM height profile at the red line in Fig. 2.7 (l). (n) Histogram of the SWCNT diameter in SC-high.

(Fig. 2.7 (a-g): Reprinted with permission from K. Kojima *et al.*, *Langmuir* **2022**, *38*, 29, 8899–8905. Copyright 2022 American Chemical Society, Fig. 2.7 (h-n): Reprinted with permission from K. Kojima *et al.*, *Applied Physics Express* **2022**, *15*, 125003. Copyright 2022 The Japan Society of Applied Physics.)

2.3.4 Concentration process of SWCNT-SC dispersions by the ultrafiltration method

To obtain the SWCNT dispersion exhibiting the LC phase, the SWCNT concentration must be increased while maintaining a good dispersion state. Figure 2.8 shows the SWCNT size distributions of SC-high before and after the concentration process by the ultrafiltration method. The distributions were almost the same, that is, the SWCNT dispersion state was maintained during the process. This approach condensed the SWCNTs in 5 hours. It is much faster than the previously reported dialysis method, which required 1–2 weeks[28].
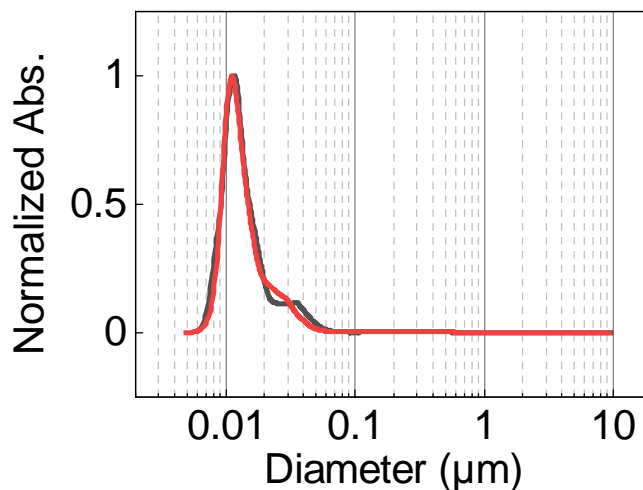

Figure 2.8 The SWCNT size distributions of SC-high before (black) and after (red) concentration process.

2.3.5 Phase transition of SWCNT-SC dispersions

Figure 2.9 (a-c) and (f-h) show POM images of SC-low and SC-high dispersion at different concentrations. The dispersions were sealed in a glass capillary to prevent drying and left to stand for a week to promote the formation of the LC phase. At low SWCNT concentrations, birefringence was not observed in SC-low, this phase is consistent with the isotropic phase (Fig. 2.9 (a)). In the isotropic phase of SC-high, birefringence was not observed except for some SWCNT agglomerates by POM observation under crossed Nicols (Fig. 2.9 (f)). At the middle concentrations, the LC phase emerged in the form of spindle-shaped LC droplets (tactoids) that coexist with the isotropic phase in both dispersions (Fig. 2.9 (b, g))[16,21,23,24,27,28,39-41]. The number of tactoids increased as SWCNT concentration became high. When the dispersions were further concentrated, the fully covered birefringence indicated the nematic phase appeared (Fig. 2.9 (c, h)).

Figure 2.9 (d, i) show the LC phase diagrams of SC-low and SC-high dispersion. The phase transition concentrations from isotropic phase to biphasic state ($\phi_{iso\sim bip}$) and from biphasic state to nematic phase ($\phi_{bip\sim nem}$) were estimated by the sigmoid curve fitting (Fig. 2.9 (e, j)). Here, the isotropic phase, biphasic state, and nematic phase were set to be 0, 0.5, and 1 on the vertical axis. The sigmoid curve fitting was conducted by

$$y = \frac{-1}{1 + e^{(x-x_0)/dx}} \tag{Eq. 2.2}$$

The fitting results were indicated by black solid lines in Fig. 2.9 (e, j). The transition concentrations from the isotropic phase to the biphasic state, and from the biphasic state to the nematic phase were estimated at the points of 0.25 and 0.75, respectively. The obtained $\phi_{iso\sim bip}$ and $\phi_{bip\sim nem}$ were ~0.24 vol% and ~0.32 vol% for the SC-low dispersion, and ~0.16 vol% and ~0.27 vol% for the SC-high dispersion, respectively. The phase transition concentrations of SC-high are lower than those for the SC-low dispersion. This tendency is explainable by Onsager theory which can predict the isotropic-nematic phase transition for a rigid rod with length L and diameter D [42]. This theory is based on the competition between the orientational entropic contribution to the free energy and the excluded-volume potential. As the concentration increases, the free rotational motion of the rod-like particles is restricted. At a critical concentration, alignment spontaneously occurs because a larger translational entropy can be obtained even if the rotational entropy is lost. According to the Onsager theory, the phase transition concentration is inversely proportional to L/D; $\phi_{iso\sim bip}$ = 3.34 D/L and $\phi_{bip\sim nem}$ = 4.49 D/L [42]. Therefore, the differences between the transition concentrations of SC-high and SC-low can be ascribed to the difference in L/D.

On the other hand, the theory predicts much higher transition concentrations ($\phi_{iso\sim bip}$ = 0.50 vol% and $\phi_{bip\sim nem}$ = 0.68 vol% for SC-low and $\phi_{iso\sim bip}$ = 0.31 vol% and $\phi_{bip\sim nem}$ = 0.41 vol% for SC-high). The effect of van der Waals force on the SWCNT LC phase transition concentration has been investigated in detail[43]. The surface of SWCNTs was protonated by superacid, which causes electrostatic repulsion between SWCNTs. When the degree of protonation is small (so the electrostatic repulsive force is small), a phase transition occurs at a concentration less than the theoretically predicted one. As protonation increases, the electrostatic repulsive force becomes larger. Consequently, the phase transition occurs at a concentration close to the theoretically predicted value. In the DLVO theory, the attractive force (van der Waals force) and the electrostatic repulsive force dominate the colloid stability. When the two colloidal particles approach each other, they are stabilized at a distance where the particles keep dispersing under negative potential energy. Thus, the degree of protonation affects the phase transition

concentrations. Therefore, the discrepancy between the theory and the experimental results in SC-low and SC-high is attributed to the attractive interaction between SWCNTs.
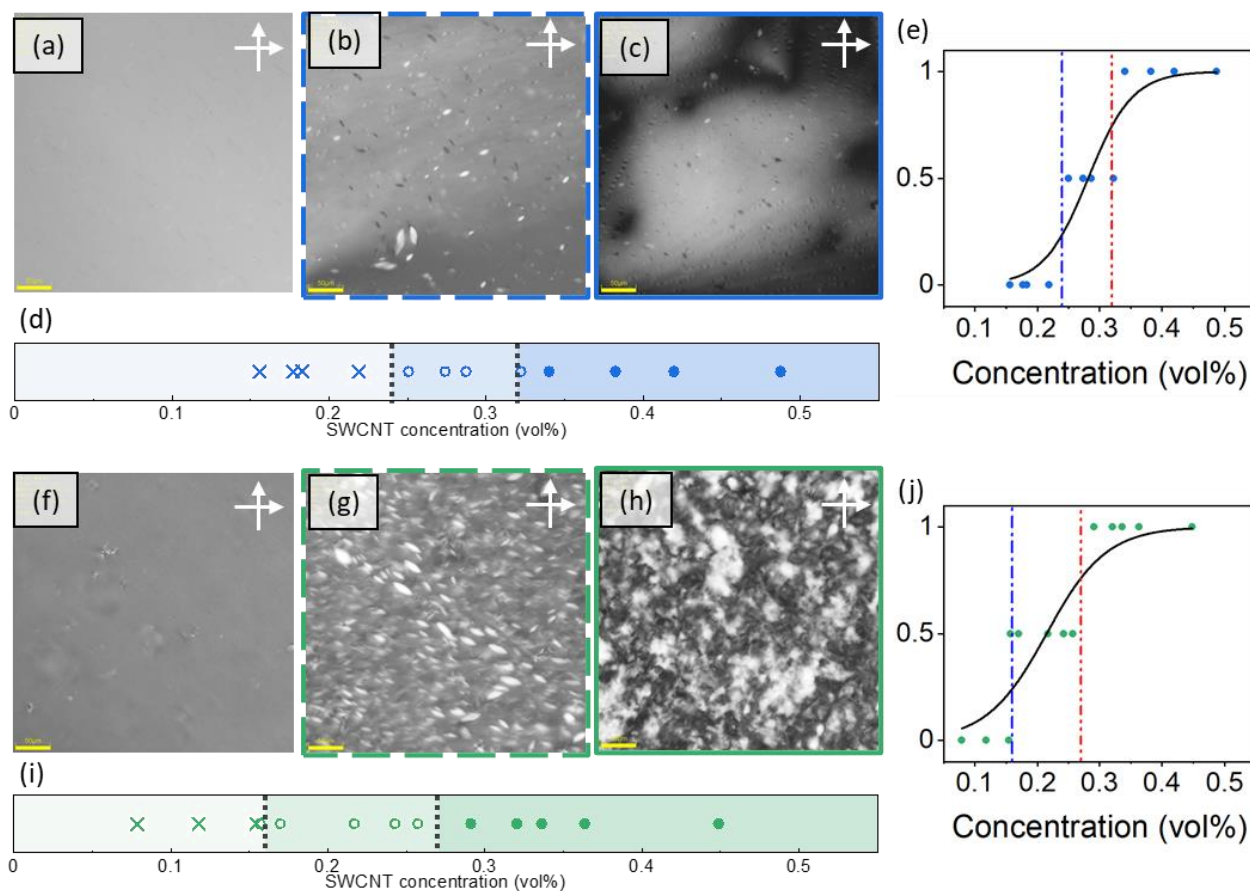

Figure 2.9 (a-c) POM images of SC-low ((a)Isotropic phase: 0.16 vol%, (b) Biphasic state: 0.27 vol%, and (c) Nematic phase: 0.49 vol%). Scale bars are 50 µm. (d) The LC phase diagram of SC-low. Cross marks, open circles and filled circles indicate isotropic phase, biphasic state, and nematic phase, respectively. (e) Sigmoid curve fitting for SC-low. (f-h) POM images of SC-high ((f)Isotropic phase: 0.12 vol%, (g) Biphasic state: 0.17 vol%, and (h) Nematic phase: 0.44 vol%). Scale bars are 50 µm. (i) The LC phase diagram of SC-high. The symbols are same as Fig. 2.9 (d). (j) Sigmoid curve fitting for SC-high.

(Fig. 2.9 (b): Reprinted with permission from K. Kojima *et al.*, *Langmuir* **2022**, *38*, 29, 8899–8905. Copyright 2022 American Chemical Society, Fig. 2.9 (e-h, j): Reprinted with permission from K. Kojima *et al.*, *Applied Physics Express* **2022**, *15*, 125003. Copyright 2022 The Japan Society of Applied Physics.)

2.3.6 LC domain size of SWCNT-SC dispersion

The uniform brightness birefringent domain in the nematic phase confirmed the presence of a well-aligned director field, which can be related to a fully developed single LC phase. Comparing the nematic phase of the dispersions, SC-low dispersion exhibited larger LC domains than SC-high (Fig. 2.10). There are two possible reasons. The first reason is large agglomerate in SC-high dispersion (Fig. 2.7 (h, i)). In previous research, the purification of rod-like SWCNTs achieved the wide SWCNT orientation[22]. Therefore, it is assumed that the agglomerates of SC-high disturbed the LC phase. In the second reason, according to the studies on the multi-walled CNT (MWCNT) dispersions with the different L and D, the larger LC domains were more often observed in the large D MWCNT dispersion[44]. This is probably because MWCNTs with large D have larger cross-sections and thus higher rigidity than the smaller D MWCNTs. In the same way, the larger D SWCNTs in SC-low dispersion may cause larger LC domain sizes.
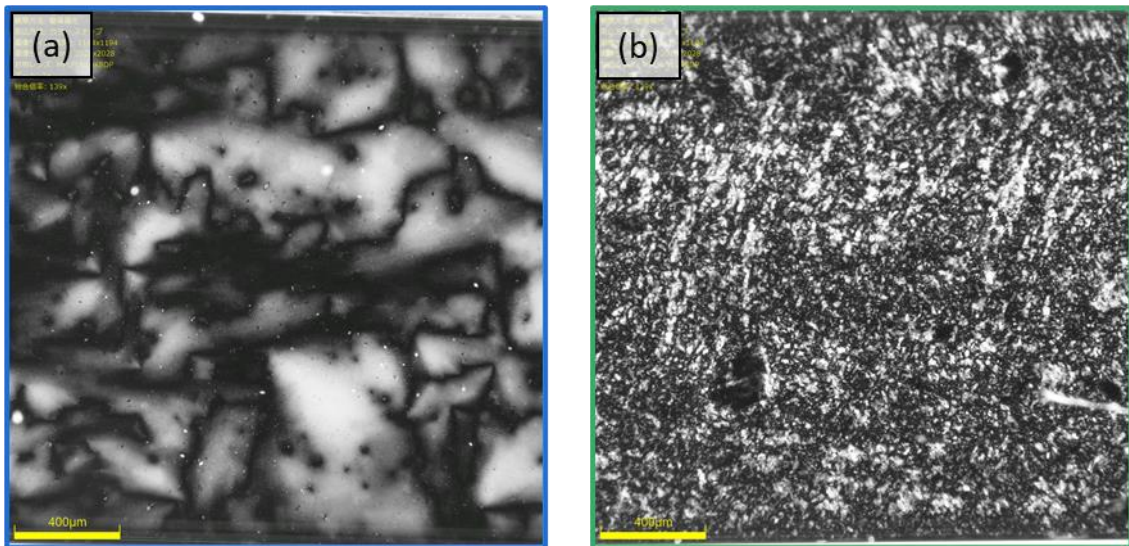

Figure 2.10 Wide-range POM images of (a) SC-low and (b) SC-high. Scale bars are 400 µm.

2.3.7 Aligned SWCNT films prepared from SWCNT-SC dispersions

To evaluate the effect of LC phase on SWCNT alignment in materials, the SWCNT films were prepared by the simple bar coating from the SC-low and SC-high dispersions. The SWCNT concentrations of SC-low and SC-high were 0.49 vol% and 0.44 vol%. Strong optical anisotropies were demonstrated on a cm-scale for SC-low (Fig. 2.11 (a, b)) and SC-high (Fig. 2.11 (c, d)) film. The black domains in Fig. 2.11 (d) were the SWCNT agglomerates that equivalented to the large agglomerates (Fig. 2.7 (h, i)) or occurred during the concentration process. We measured the optical absorption spectra of the films by changing the sample angle from 0° to 90° in each 10°. Figure 2.11 (e, f) show absorption spectra under different sample angles from 0° to 90° in each 10°. The direction of the polarizer was parallel to the shear direction of the sample at 0°. From the absorption spectra, the two-dimensional nematic order parameters S_{2D} were calculated by

$$S_{2D} = \frac{A_{\parallel} - A_{\perp}}{A_{\parallel} + 2A_{\perp}} \qquad \text{(Eq. 2.3)}$$

where $A_{\parallel}$ and $A_{\perp}$ are the absorption intensities at 735 nm at 0° and 90°. The S_{2D} values of films were ~0.14 in SC-low (L/D = 665) and ~0.22 in SC-high (L/D = 1088), respectively. A similar L/D dependence was reported in rod-like cellulose nanocrystal (CNC) films[45,46]. Under the shear flow, the CNC with higher L/D tends to align to decrease the stress on CNC. Because of shape anisotropy, non-spherical particles (high L/D) hinder their rotational motions. Therefore, producing the SWCNTs with large L/D is effective to obtain highly oriented SWCNT materials.
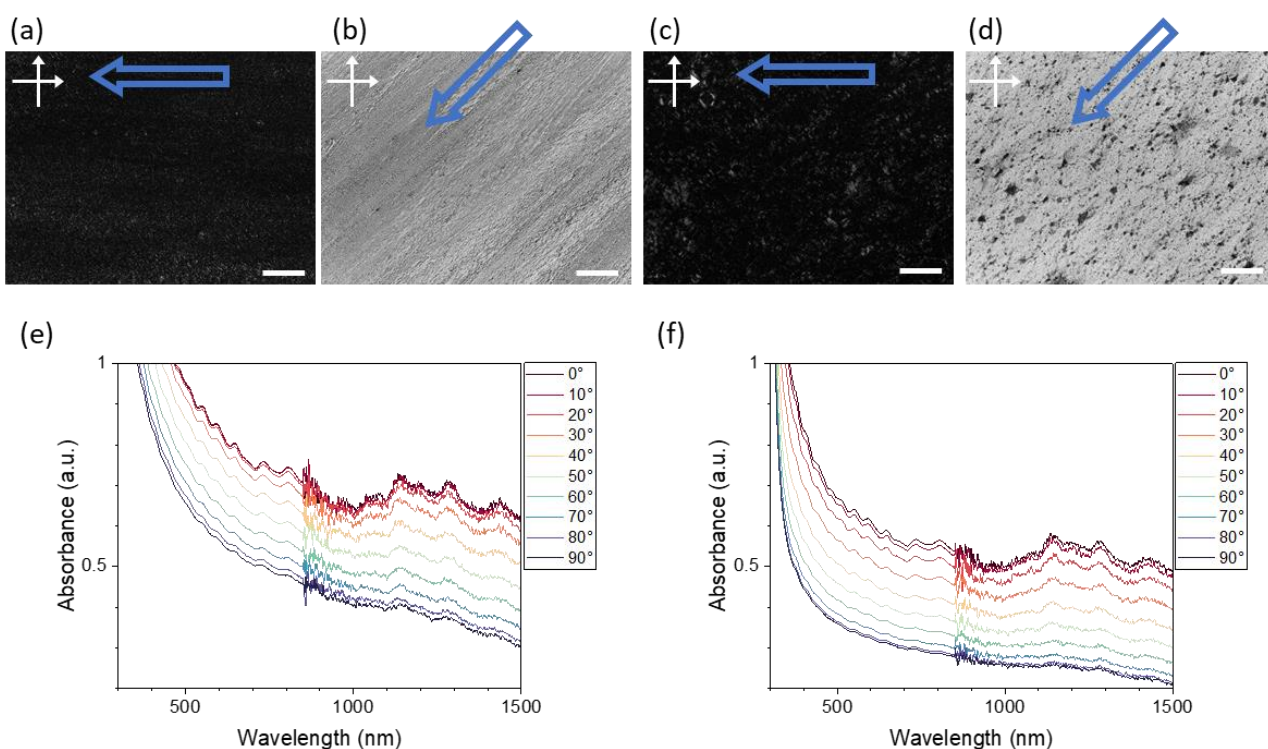

Figure 2.11 POM images of the film of (a, b) SC-low and (c, d) SC-high dispersions at (a, c) 0º and (b, d) 45º under crossed polarizers (white double arrows). Blue outlined arrows indicate the shear directions of the bar coating. Scale bars are 200 µm. Polarized optical absorption spectra of the film of (e) SC-low and (f) SC-high dispersions with different sample angles, 0° - 90°.

2.4   Conclusion

In this chapter, to obtain SWCNT dispersions that contain rod-like SWCNTs, optimization of dispersion conditions and comparing different types of SWCNT were conducted. A well-dispersed state was successfully prepared with sodium cholate by probe sonicator, which was monitored and confirmed by optical microscope observations and centrifugal sedimentation analysis (DCS analysis). Additionally, by comparing the dispersions of several SWCNTs which prepared by optimized dispersion processes, it is likely that SWCNTs with high crystallinity, such as eDIPS and Tuball, are suitable for preparing rod-like SWCNTs.

Ultrafiltration concentrated the SWCNTs in the dispersion without changing the dispersion states. As the SWCNT concentration increased, the isotropic phase changed to the nematic phase through the biphasic state. The transition concentrations from the isotropic phase to the biphasic state and from the biphasic state to the nematic phase of SC-high dispersion (L/D = 1088) were lower than SC-low (L/D = 665). This tendency was consistent with the Onsager theory although the theory predicts much higher transition concentrations. The difference was attributed to the strong van der Waals interaction between SWCNTs.

In the nematic phase, the larger D SWCNTs in SC-low dispersion caused larger LC domain sizes. On the other hand, the more aligned SWCNT film was obtained by the simple bar coating of the larger L/D SC-high dispersion. Consequently, preparation of the dispersion with large L/D SWCNTs is quite important to produce highly oriented SWCNT materials.

Chapter 3　Effect of surfactant species on SWCNT liquid crystalline behaviors

3.1　Introduction

　　A lot of substance has been reported as suitable dispersants for SWCNTs, for example, surfactants, DNA, and polymers. Naturally, each dispersant has different dispersibility for SWCNTs. Consequently, better electrical and mechanical properties of the wet-spun CNT fibers were reported using the sodium taurodeoxycholate (TDOC) dispersions, as compared with the other cholate derivatives such as SC and sodium deoxycholate (SDOC)[47]. It is plausible that the difference in dispersant caused the difference in the alignment of SWCNTs. Hence, it is also considered that the phase transition behaviors are affected by dispersants.

　　In this section, we prepare SWCNT dispersions with the aid of cholate derivatives. Through the comparison of the LC phase of the dispersions with SDOC, TDOC, and SC (Chapter 2), we investigate the effect of dispersant species on phase transition behavior.

3.2 Experimental section

3.2.1 Preparation of the surfactant-stabilized SWCNT dispersions

The preparation procedures for the SWCNT dispersions were almost the same as the method of section 2.2.4. We used the same SWCNT powder purchased from Meijo nanocarbon (eDIPS EC-DX, Lot. 5R79I25C). Sodium deoxycholate (SDOC) (Wako), and sodium taurodeoxycholate (TDOC) (Nacalai Tesque Inc.) were used as dispersants.

3.2.2 Estimation of SWCNT dispersion states and size measurement of SWCNTs

The procedure is the same as in section 2.2.2. and 2.2.5.

3.2.3 Calculation of concentration of SWCNT dispersions

The concentrations of SWCNT dispersions with SDOC and TDOC were calculated from the calibration curve (Fig. 2.2 and Eq. 2.1) which was prepared by SWCNT-SC dispersion.

3.2.4 Observations of LC phases

The procedure is the same as in section 2.2.6.

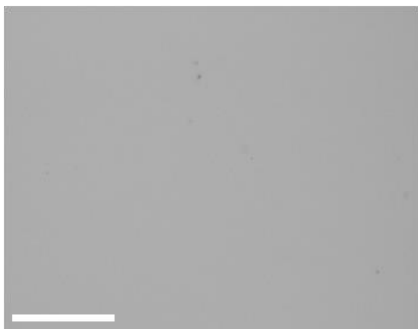### 3.2.5 Measurements of surface condition of SWCNTs

To compare surface conditions of SWCNT with different dispersions, Raman shifts of G-band (in-plane vibration mode of aromatic carbons) and ζ potentials of SC-low, SC-high, SDOC, and TDOC dispersions were measured. Raman measurements of the dispersions were carried out by a 532 nm laser (HORIBA, T64000). Additionally, we also measured ζ potentials of SWCNT dispersions in a disposable cell (Malvern Panalytical, DTS1070) by the ζ potential analyzer (Malvern Panalytical, ZETASIZER nano ZS).
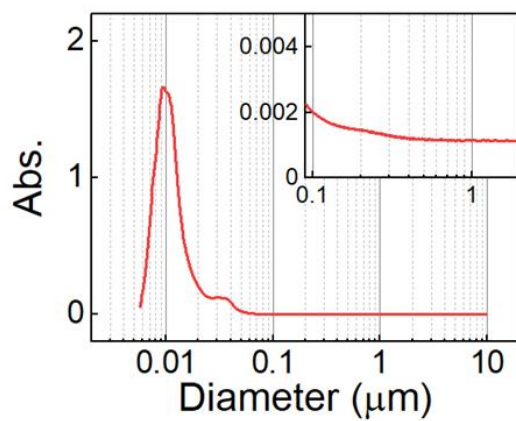
3.3   Results and discussion

3.3.1   Size estimations of SWCNTs in SWCNT-SDOC/TDOC dispersions

Figure 3.1 (a, h) show the optical microscope images of the SDOC and TDOC dispersions. The agglomerates in micrometer size were hardly observed. SWCNT size distributions in the SDOC and TDOC dispersions were measured by DCS (Fig. 3.1 (b, i)). The intense single peak at 9.5 nm and 10.5 nm were observed for the SDOC and TDOC dispersions. The length and diameter of SWCNTs were measured by SEM and AFM. Figure 3.1 (c, e) show the SEM and AFM observations of SDOC dispersions, and Fig. 3.1 (f) shows the AFM height profile at the red line in Fig. 3.1 (e). From the distributions of SWCNT length and diameter in the SDOC dispersion (Fig. 3.1 (d, g)), the average values were $L = {\sim}1.1$ μm and $D = {\sim}2.0$ nm, respectively. Thus, the aspect ratio L/D of SWCNT in SDOC is 549. In addition, Figures 3.1 (j, l) and 3.1 (m) show the SEM and AFM observations and AFM height profile of TDOC dispersion. From the distributions of SWCNT length and diameter in TDOC (Fig. 3.1 (k, n)), the average values were $L = {\sim}1.2$ μm and $D = {\sim}2.0$ nm, respectively. Hence, the aspect ratio L/D of SWCNT in TDOC is 601. In addition, the Stokes diameters of rod-like particles were calculated to be 5.3 nm in SDOC and 5.2 nm in TDOC by Eq. 1.3. These values were comparable with the DCS measurements (Fig. 3.1 (b, i)).
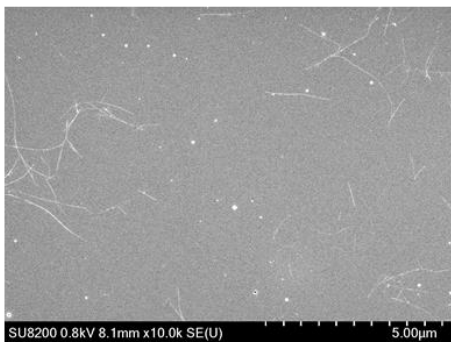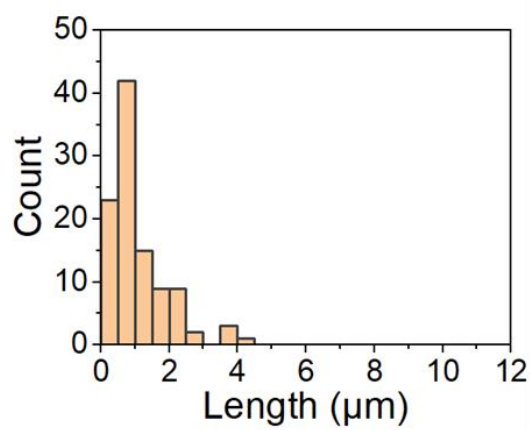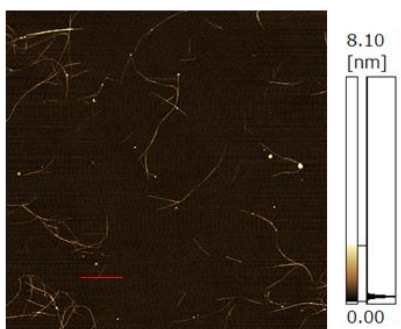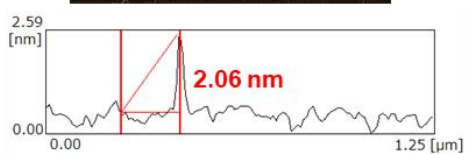
(a)

(b)

(c)

SU8200 0.8kV 8.1mm x10.0k SE(U)   5.00μm

(d)

(e)

8.10
[nm]

0.00

(f)

2.59
[nm]

2.06 nm

0.00

0.00   1.25 [μm]
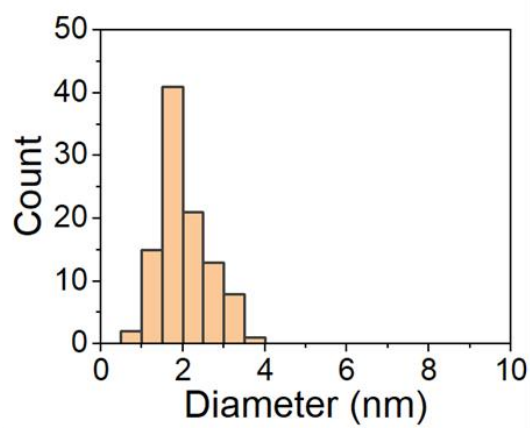
(g)
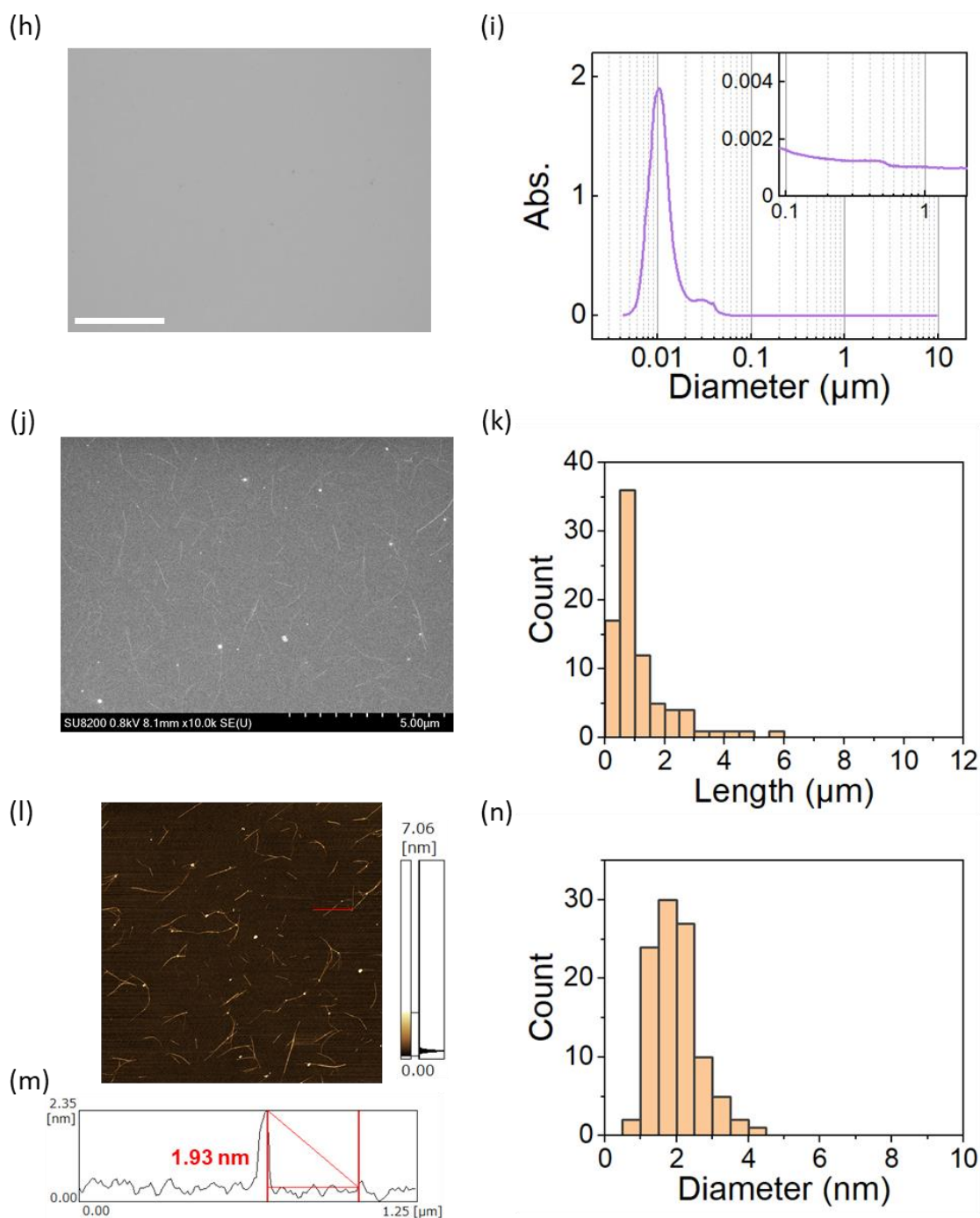
Figure 3.1 (a) A typical optical microscope image of SDOC. Scale bar is 100 μm. (b) The SWCNT size distribution of SDOC. (c) A typical SEM image. (d) Histogram of SWCNT length in SDOC from SEM. (e) A typical AFM image. The size of the image is 10 μm square. (f) AFM height profile at the red line in Fig. 3.1 (e). (g) Histogram of SWCNT diameter in SDOC from AFM. (h) A typical optical microscope image of TDOC. Scale bar is 100 μm. (i) The SWCNT size distribution in TDOC. (j) A typical SEM image. (k) Histogram of SWCNT length in TDOC from SEM. (l) A typical AFM image. The size of the image is 10 μm square. (m) AFM height profile at the red line in Fig. 3.1 (l). (n) Histogram of the SWCNT diameter in TDOC. (Reprinted with permission from K. Kojima *et al.*, *Applied Physics Express* **2022**, *15*, 125003. Copyright 2022 The Japan Society of Applied Physics.)

3.3.2 Phase transitions of SWCNT dispersions

Figure 3.2 shows the POM images at different SWCNT concentrations and the phase diagrams of the SDOC and the TDOC dispersions. POM observations indicate the isotropic phase, biphasic state, and nematic phase with increasing the SWCNT concentrations. The phase transition concentrations were estimated in the same way as in section 2.3.5. The values of $\phi_{iso \sim bip}$ and $\phi_{bip \sim nem}$ were estimated to be ~0.29 vol% and ~0.42 vol% for the SDOC sample, and ~0.31 vol% and ~0.34 vol% for the TDOC sample, respectively (Fig. 3.2 (e, j)). The values of L/D of SDOC and TDOC were close, therefore, phase transition concentrations were not affected by the influence of L/D derived from Onsager theory[42].
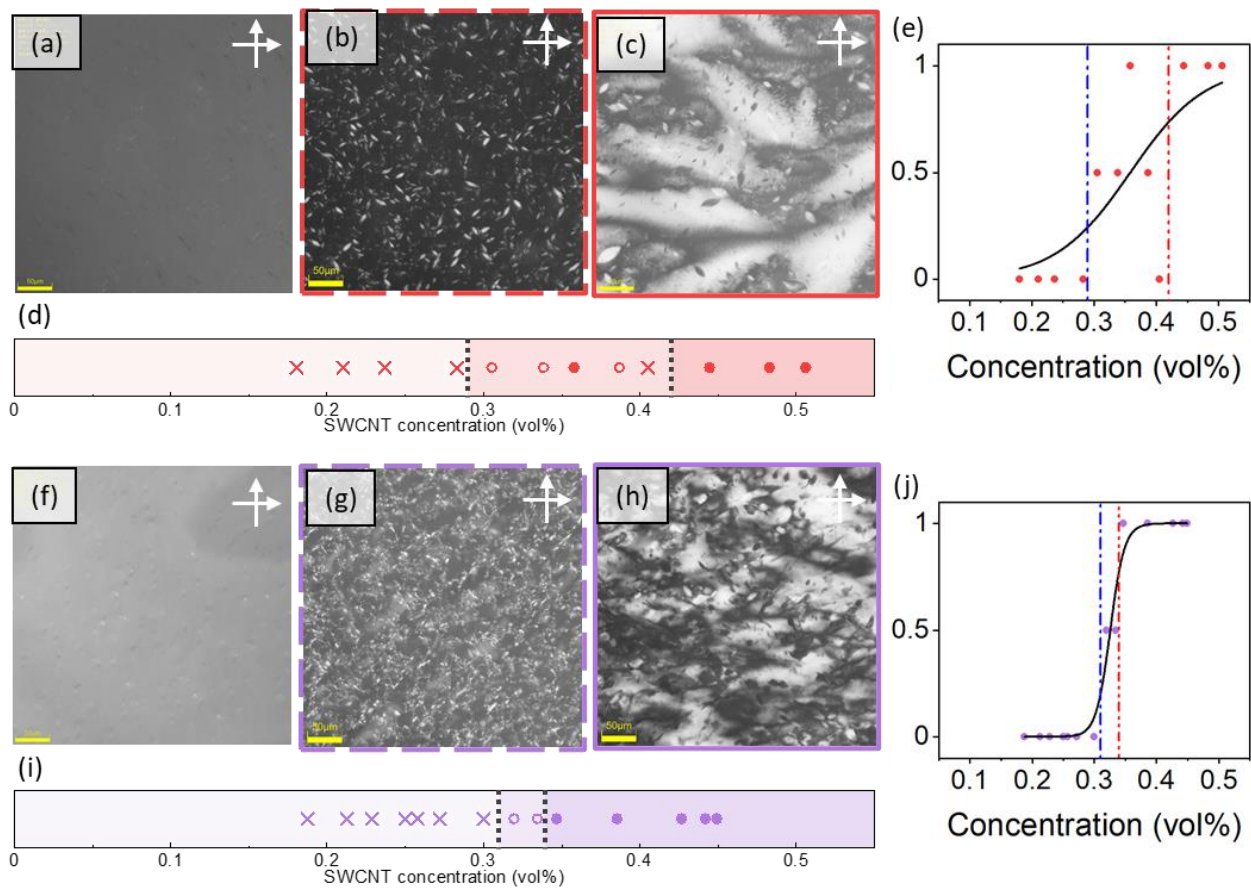
Figure 3.2 (a-c) POM images of SDOC ((a)Isotropic phase: 0.18 vol%, (b) Biphasic state: 0.39 vol%, and (c) Nematic phase: 0.51 vol%). Scale bars are 50 μm. (d) The LC phase diagram of SDOC. Cross marks, open circles, and filled circles indicate the isotropic phase, biphasic state, and nematic phase, respectively. (e) Sigmoid curve fitting for SDOC. (f-h) POM images of TDOC ((f)Isotropic phase: 0.19 vol%, (g) Biphasic state: 0.33 vol%, and (h) Nematic phase: 0.44 vol%). Scale bars are 50 μm. (i) The LC phase diagram of TDOC. The symbols are the same as in Fig. 3.2 (d). (j) Sigmoid curve fitting for TDOC. (Reprinted with permission from K. Kojima *et al.*, *Applied Physics Express* **2022**, *15*, 125003. Copyright 2022 The Japan Society of Applied Physics.)

3.3.3 Comparison of the phase transition concentrations of SDOC, TDOC, and SWCNT-SC dispersions

Figure 3.3 (a) shows the plot of $\phi_{iso\sim bip}$ and $\phi_{bip\sim nem}$ of SC-high, SC-low, SDOC, and TDOC dispersions against SWCNT aspect ratio, *L/D*. To check the surface charge states of the SWCNTs, the ζ potential and the resonance Raman measurements were carried out. The obtained ζ potentials were -41.1 ± 2.65, -46.5 ± 3.74, -58.2 ± 1.63, and -58.3 ± 3.77 mV for the SC-high, SC-low, SDOC, and TDOC samples (Fig. 3.3 (b-e)). It is worth mentioning that the ζ potentials of SC-high and SC-low are almost the same within the experimental errors whereas the SDOC and TDOC samples show significantly higher values. On the other hand, the peak positions of the G-bands of SWCNTs which indicated a charge transfer of SWCNT such as protonation were almost the same for all samples ($\sim$1594 cm^{-1}) (Fig. 3.3 (f)). Therefore, the difference of ζ potentials was derived from the difference of dispersants.

The different transition concentrations between SC-high and SC-low are likely attributed to the different *L/D*. On the other hand, despite the error bars of *L/D* in SDOC, TDOC, SC-low overlapped, the estimated $\phi_{iso\sim bip}$ and $\phi_{bip\sim nem}$ of the SDOC and the TDOC samples are slightly higher than those of SC-low ($\phi_{iso\sim bip}$ and $\phi_{bip\sim nem}$ were $\sim$0.24 vol% and $\sim$0.32 vol%). It is assumed that the stronger repulsive forces derived from the ζ potentials cause higher transition concentrations of SDOC and TDOC dispersions.

Meanwhile, the SWCNT fibers have been produced by the wet spinning of cholate-assisted SWCNT aqueous dispersions[9,47]. Among these dispersions, the SWCNT fibers from the TDOC dispersion showed better electrical and mechanical properties than the other bile salt derivatives such as SC, SDOC, sodium ursodeoxycholate, sodium glycocholate, sodium taurocholate, and sodium hyodeoxycholate[47]. The present findings indicate that TDOC is not a special dispersant from the viewpoint of the LC properties. The superiority of TDOC observed in the wet-spun SWCNT fibers may be because TDOC has a higher dispersibility than other cholates, reducing dispersion time, and further maintaining the CNT lengths[47].
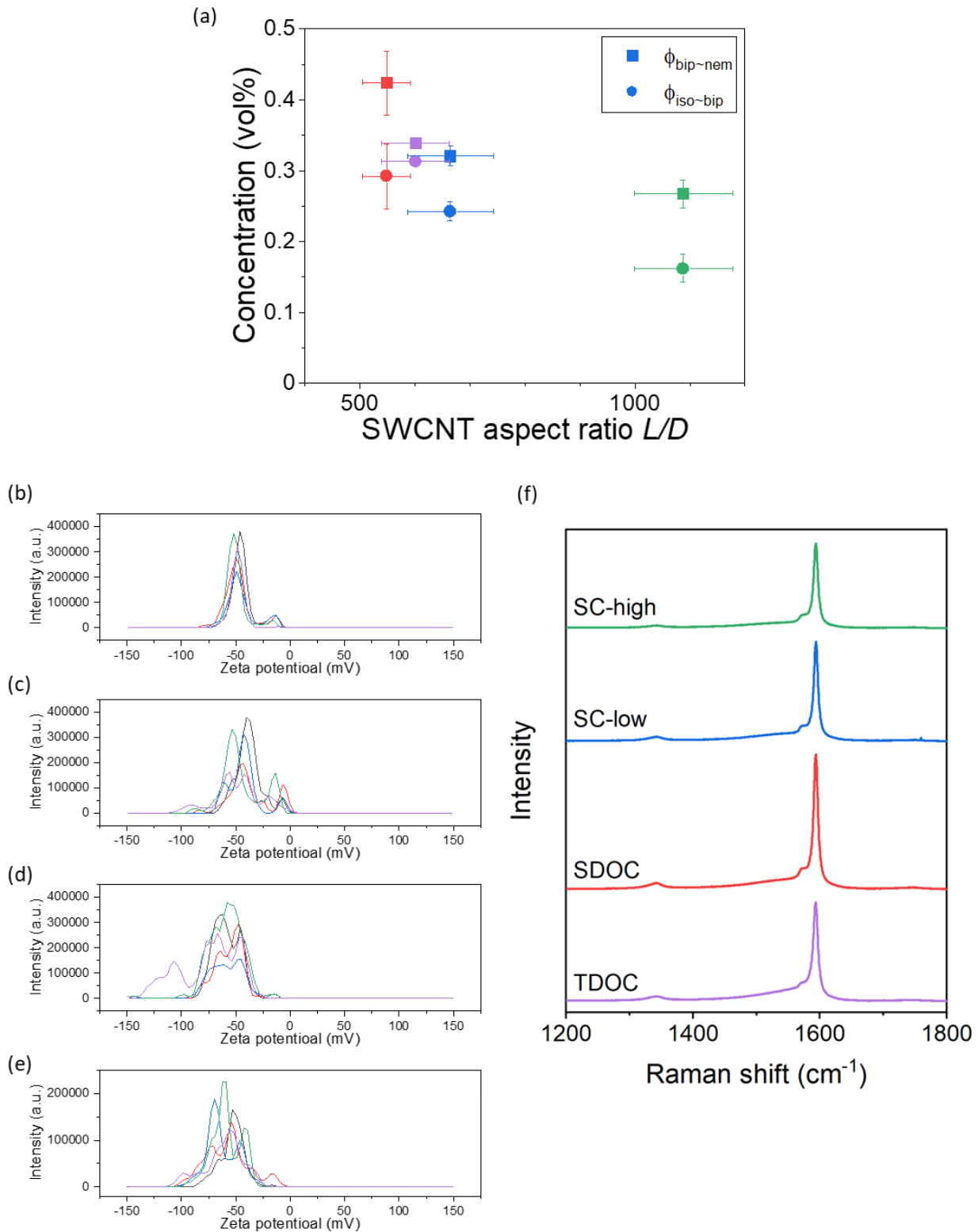
Figure 3.3 (a) The plot of phase transition concentrations, $\phi_{iso\sim bip}$ and $\phi_{bip\sim nem}$, of SC-high, SC-low, SDOC, and TDOC dispersions against SWCNT aspect ratio. The ζ potential distributions of (b) SC-high, (c) SC-low, (d) SDOC, and (e) TDOC. (f) Raman spectra of SC-high (green), SC-low (blue), SDOC (red), and TDOC (purple) dispersions. (Fig. 3.3 (f): Reprinted with permission from K. Kojima *et al.*, Applied Physics Express **2022**, *15*, 125003. Copyright 2022 The Japan Society of Applied Physics.)

3.3.4 LC domain size of SDOC, TDOC, and SWCNT-SC dispersions

Figure 3.4 (a-d) show the nematic phase of SC-low, SDOC, TDOC, and SC-high, which were lined up from largest LC domain to smallest. Table 3.1 lists SWCNT diameter D, length L, aspect ratio L/D, and ζ potential of each dispersion. As described in section 2.3.6, the larger D of CNTs tends to cause a larger domain size in the CNT nematic phases[44]. Because D of SWCNTs in the SDOC, TDOC and SC-high dispersions are smaller than that of SC-low, the SDOC and TDOC (also SC-high) dispersions may show smaller birefringence in the whole area.
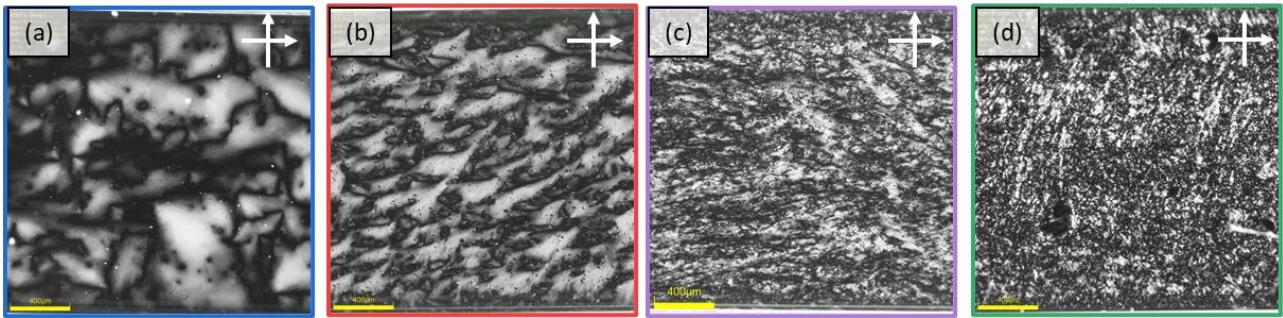
Figure 3.4 Wide-range POM images of (a) SC-low (Same as Fig. 2.10 (a)), (b) SDOC, (c) TDOC, and (d) SC-high (Same as Fig. 2.10 (b)). Scale bars are 400 μm.

Table 3.1 The parameters of each dispersion.

Sample	Diameter D [nm]	Length L [μm]	SWCNT aspect ratio L/D	ζ potential [mV]
SC-low	2.8 ± 0.26	1.9 ± 0.13	665 ± 78.4	-41.1 ± 3.74
SDOC	2.0 ± 0.06	1.1 ± 0.08	549 ± 43.5	-58.2 ± 1.63
TDOC	2.0 ± 0.06	1.2 ± 0.12	601 ± 62.4	-58.3 ± 3.77
SC-high	1.5 ± 0.08	1.7 ± 0.11	1088 ± 90.3	-46.5 ± 2.65

3.4 Conclusion

In this chapter, the effect of the surfactants on the LC phase behavior of the well-dispersed cholate-based SWCNT dispersions was investigated. Regardless of dispersant species, liquid crystalline SWCNT dispersions were prepared, and the isotropic phase, biphasic state, and nematic phase were observed as increasing the SWCNT concentrations. The phase transition concentrations, $\phi_{iso\sim bip}$ and $\phi_{bip\sim nem}$ of the SDOC and the TDOC samples were slightly higher than that of the SC-low sample, which may result from the lower ζ potentials. Furthermore, the LC domain sizes became larger as SWCNT diameter D became larger.

Chapter 4   SWCNTs orientations in biphasic states and nematic phase

4.1   Introduction

Although liquid crystalline SWCNT dispersions show characteristic LC phase, the study of SWCNT orientation in a liquid state has been limited. In this chapter, the orientations of SWCNTs in biphasic states and nematic phase are discussed.

In a biphasic state, the nematic droplets were floated in the isotropic phase, and they are called "tactoid." Tactoids are classified into two or three groups by the SWCNT orientation[39-41]. The tactoid morphology of amyloid fiber has been investigated from the viewpoint of the amyloid fiber length[48], whereas there are no reports of the CNT length dependence of the tactoid morphologies. Therefore, in this chapter, the relationship between the tactoid morphology and SWCNT dispersion condition is examined by comparing SWCNT/SC, SDOC, and TDOC dispersions.

Generally, the nematic phase exhibits characteristic textures. In the nematic phase of SWCNT dispersions, defects of liquid crystal called the Schlieren texture have been observed[18,23]. The SWCNT orientations in the Schlieren texture were observed at the condition of the dried film. However, they haven't been observed at the liquid phase in detail. Defects of liquid crystal in the nematic phase of SC-low dispersion are observed in detail.

4.2   Materials and methods

4.2.1   Overview of SWCNT dispersions

The tactoids in biphasic states of SC-high, SC-low, SDOC and TDOC dispersions and the Schlieren textures in the nematic phase of SC-low were observed. The sample preparations were described in chapter 2 and 3.

4.2.2   Observation of polarized optical microscopy with tint plate

The procedure of sample preparations is the same as in section 2.2.6. To confirm the SWCNT orientations in LC phases, we used a cross-polarized light microscope (OLYMPUS, DSX510 and BX51) and a first-order retardation plate (sensitive tint plate) (OLYMPUS, U-TP530).

POM with a first-order retardation plate can directly observe the SWCNT arrangements by the difference of color. When polarized light goes through an orientated sample, the light is divided into two waves along the fast axis and the slow axis of samples. Generally, the slow axis is the same direction as material orientation. The phase shift between the lights along each axis is called retardation R, which is indicated by sample thickness d and refractive index n

$$R = d(n_2 - n_1) \qquad \text{(Eq 4.1)}$$

where d is a sample thickness and n_1 and n_2 are the refractive indices along the fast axis and the slow axis. Figure 4.1 shows an interference color chart in which the y-axis indicates retardation of optical retardation. Depending on the value of retardation, the interference color is observed. A first-order retardation plate has a fixed phase shift along the slow axis and a fixed optical path difference is 530 nm. Therefore, the non-oriented sample, which has no birefringence under POM observation, looks red-purple color (red arrow in Fig. 4.1 pointing $R = 530$ nm). When an oriented sample is observed under POM with a first-order retardation plate, the interference color change by sample direction. If the slow axis of the sample and a first-order retardation plate are parallel (additive position), the retardation becomes larger than 530 nm. Therefore, the interference color becomes bluish color when the direction of sample orientation is parallel to the axis of a first-order retardation plate. On the other hand, if the slow axis of the sample and a first-order retardation plate are orthogonal (subtractive position), the retardation becomes smaller than 530 nm. Therefore, the interference color becomes orangish color when the direction of sample orientation is orthogonal to the axis of a first-order retardation plate. In consequence, sample orientation can be estimated by comparing the interference colors from sample observation at different degrees.
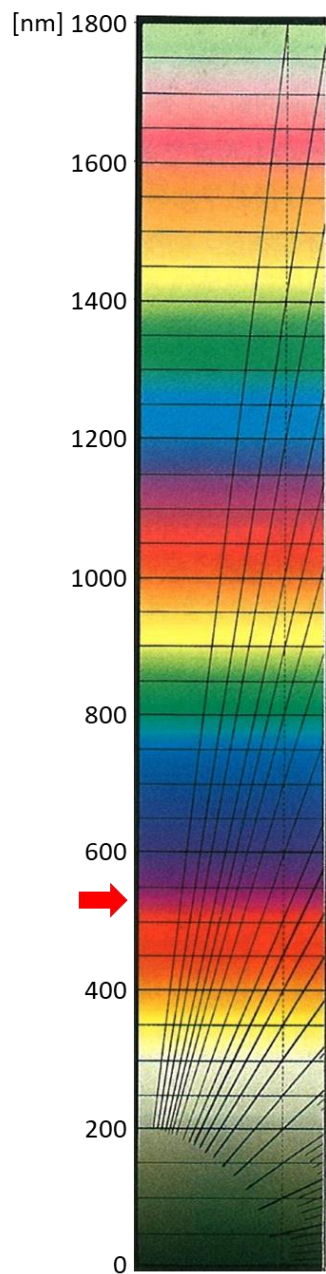
Figure 4.1 An interference color chart[49] . The red arrow pointed R = 530 nm. (Reprinted with permission from H. Awaya, *Koubunshisozai no Henkoukenbikyou Nyuumon (Isagoge of polarized optical microscope for polymers)*; AGNE Gijutsu Center Inc.: Tokyo, 2001. Copyright 2001 AGNE Gijutsu Center Inc.)

4.3 Results and discussion

4.3.1 Nematic droplets in biphasic states: Tactoid

In the biphasic state, tactoids were appear in all dispersions (Fig. 4.2 (a-d)). Tactoids were classified into two groups by the constituted SWCNT orientation[39-41]. When SWCNTs are lined up along the tactoid major axis, tactoids are called homogenous tactoids (Fig. 4.2 (e)). On the other hand, when SWCNTs are lined up from one pole of the tactoid to another pole, it is called a bipolar tactoid (Fig. 4.2 (f)).
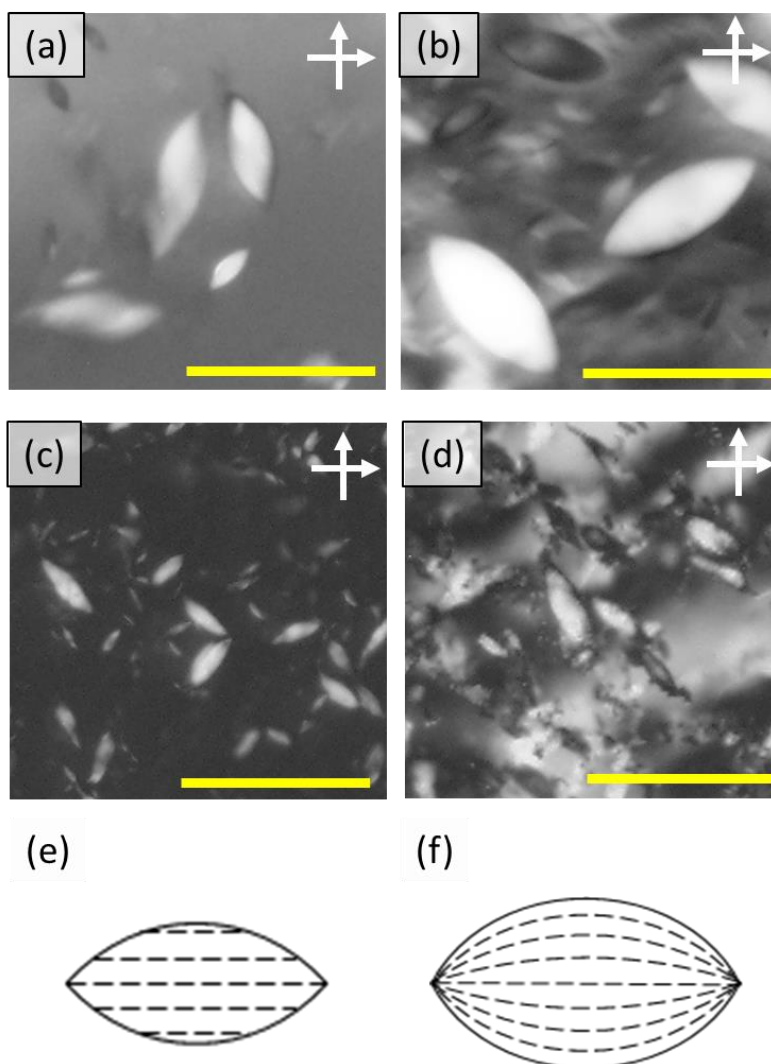

Figure 4.2 POM images with crossed Nicols of (a) SC-low (0.27 vol%), (b) SC-high (0.24 vol%), (c) SDOC (0.39 vol%), and (d) TDOC (0.35 vol%) dispersions. Scale bars are 50 μm. Schematic of (e) homogenous tactoid and (f) bipolar tactoid.

The arrangements of SWCNTs in the LC phase were directly observed by a polarized optical microscope with crossed Nicols by changing the angles of the samples. In Figure 4.3, homogenous tactoids showed bright conversions of +45° and −45°, indicating that the tactoids have different refractive indices in the long and short axes (middle row of Fig. 4.3). The images in the lower row of Fig. 4.3 were acquired with a polarized optical microscope with a tint plate inserted. The retardation of the tint plate was 530 nm, and the red arrow in Fig. 4.3 denotes the slow

axis of the tint plate. Orangish and bluish colors were observed at +45° and –45°, respectively. The bluish color indicated that the SWCNTs were oriented parallel to the slow axis of the sensitive color plate and were arranged in the long axis direction of the tactoid (upper row of Fig. 4.3).
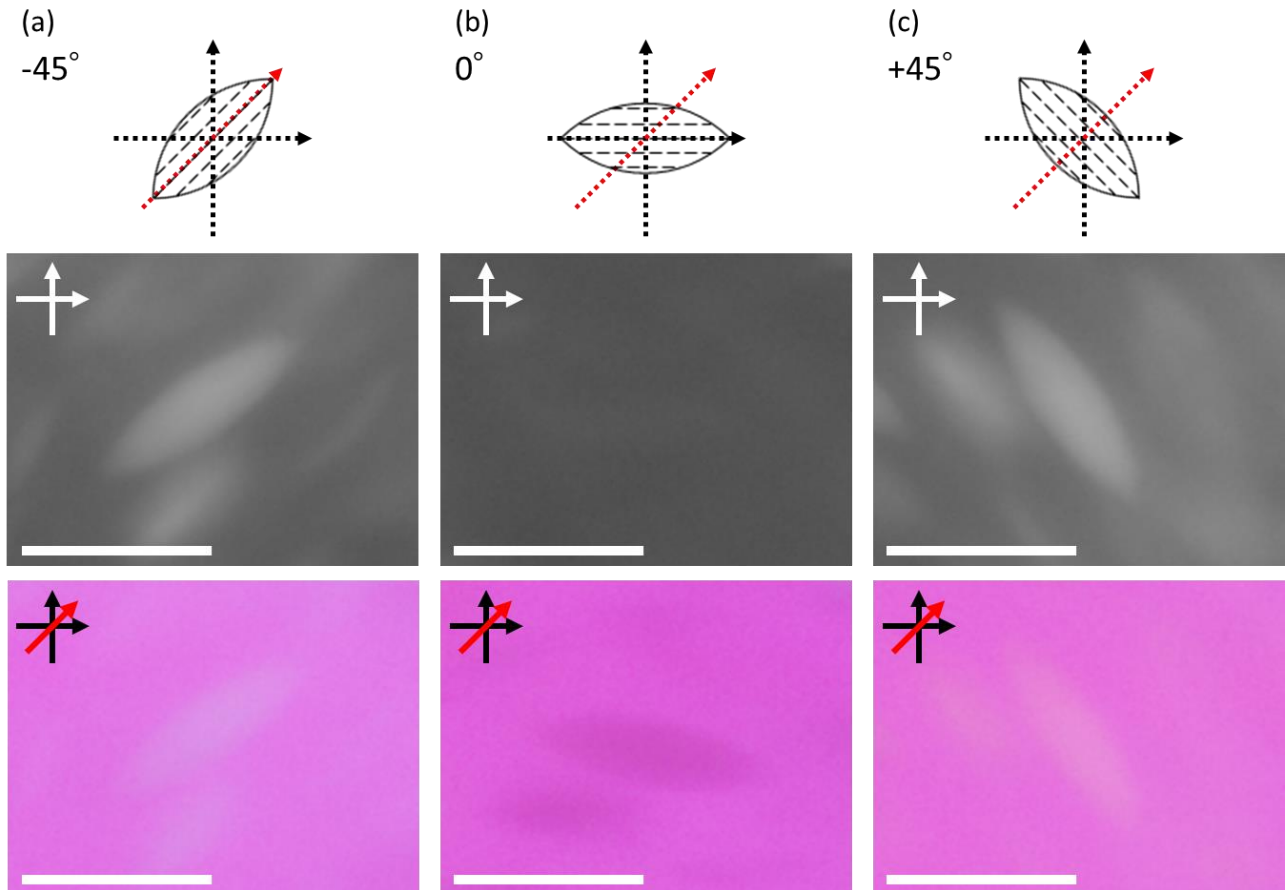

Figure 4.3 Polarized optical microscope images of homogenous tactoids with the main body axis at (a) –45, (b) 0 and (c) +45 degrees relative to the horizontal polarizer (middle row) and those with the sensitive tint plate (lower row). The optical axis of the tint plate is denoted as a red arrow. Scale bars are 20 μm.

Figure 4.4 shows the crossed Nicols optical microscope images of the bipolar tactoids. In the images with a tint plate inserted, orangish and bluish colors were observed at +45° and –45°, respectively. These observations are similar to the homogenous tactoids (Fig. 4.3). To determine the arrangements of the SWCNTs inside the bipolar tactoids, we also observed the state at different tilt angles. For a tilt angle of +10°, the lower left and the upper right of the tactoid showed an orangish color, indicating that the SWCNTs were oriented orthogonally to the slow axis of the sensitive color plate. In contrast, the SWCNTs were oriented parallel to the sensitive color plate at the upper left and the lower right of the tactoid because they appeared bluish color in the images of the –10° tilt angle. These observations are consistent with the expected SWCNT arrangement in bipolar tactoids (upper row in Fig. 4.4).
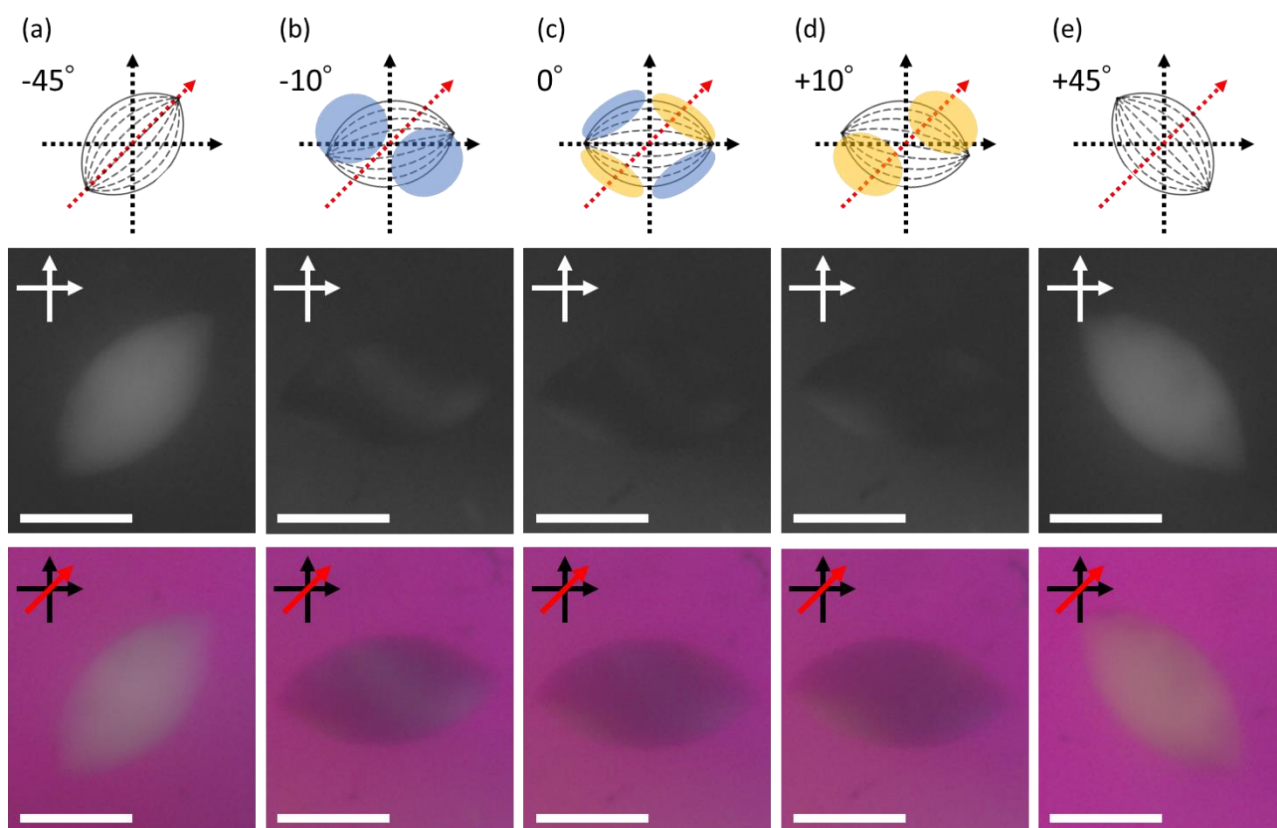
Figure 4.4 Polarized optical microscope images of bipolar tactoids with the main body axis at (a) –45, (b) –10, (c) 0, (d) +10 and (e) +45 degrees relative to the horizontal polarizer. (middle row) and those with the sensitive tint plate (lower row). The optical axis of the tint plate is denoted as a red arrow. Scale bars are 20 µm. (Reprinted with permission from K. Kojima *et al.*, *Langmuir* **2022**, *38*, 29, 8899–8905. Copyright 2022 American Chemical Society.)

From the measurement of major axis length R and minor axis length r of tactoid, tactoid aspect ratio R/r and volume $V = Rr^2$ were calculated in each tactoid. The aspect ratio of the observed tactoids is plotted as a function of the volume of the tactoids in each dispersion (Fig. 4.5). Open and filled circles indicate homogenous and bipolar tactoids. To estimate the transition volume from homogenous to bipolar tactoids, the sigmoid curve fitting was conducted (solid curves in Fig. 4.6, see Eq. (2.2)). Homogenous and bipolar tactoids are indicated by open and filled circles and set to be 0 and 1, respectively, in Fig. 4.6. The transition volumes were estimated from the points corresponding to 0.5 on the vertical axis. The transition volumes between homogenous and bipolar tactoids were estimated to be V ~4300 µm³, ~ 330 µm³, ~305 µm³, and ~637 µm³ for SC-high, SC-low, SDOC, TDOC dispersions (Fig. 4.5, 4.6). In a similar study of the amyloid fibril tactoids, a longer amyloid fibril showed a larger transition volume[48]. Regardless of the almost same L of SWCNTs in SC-high and SC-low, different V were obtained in this study. Only SWCNT aspect ratio L/D shows the same tendency, but the relational expression between L/D and V has not been expressed. Therefore, further study about SWCNT tactoids is required to address this point.
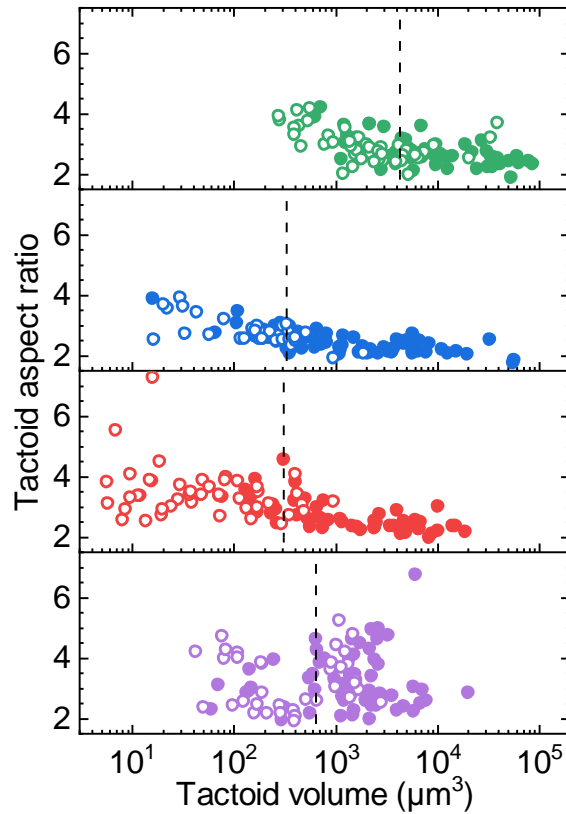
Figure 4.5 A plot of tactoid aspect ratio R/r against tactoid volume V of SC-high (green), SC-low (blue), SDOC (red), and TDOC (purple) dispersions. Open and filled circles indicate homogenous and bipolar tactoids. 100 tactoids were measured in each dispersion.
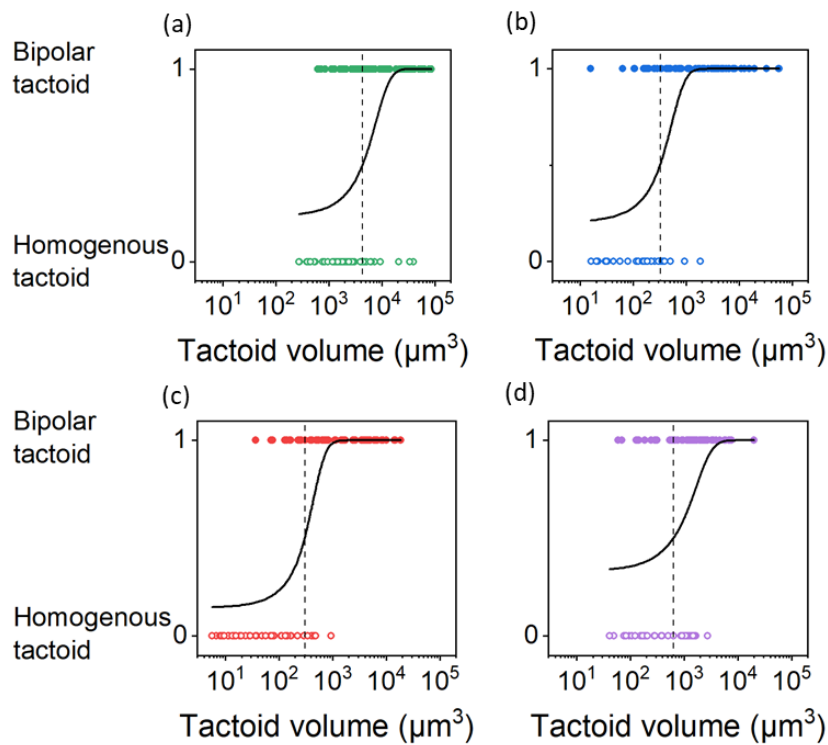

Figure 4.6 Sigmoid curve fitting of tactoid transition volume in biphasic states of (a) SC-high, (b) SC-low, (c) SDOC, and (d) TDOC dispersions. (Reprinted with permission from K. Kojima *et al.*, *Applied Physics Express* **2022**, *15*, 125003. Copyright 2022 The Japan Society of Applied Physics.)

45

For drops with a homogenous director field, the splay and the elastic energy contributions were essentially zero. Thus, the free energy is determined by the surface anchoring energy[39]. The Wulff model suggests that anchoring strength ω can be expressed as

$$\omega = \frac{1}{4}\left(\frac{R}{r}\right)^2 \ (\omega > 1) \qquad \text{(Eq. 4.2)}$$

$$\omega = \frac{R}{r} - 1 \ (0 < \omega < 1) \qquad \text{(Eq. 4.3)}$$

where R and r are the major axis length and the minor axis length of the tactoid, respectively[39]. The calculated anchoring strength of the homogenous tactoid was plotted in each dispersion (Fig. 4.7 (a)). The average values were classified into two groups, SC-high and SC-low which ω are ~2, and SDOC and TDOC which ω are ~3. Although the error ranges of them were overlapped, the classification of anchoring strength is the same as that of the ζ potentials (section 3.3.3). The anchoring strength ω might be correlated with the repulsive force (Fig. 4.7 (b)). This hypothesis is indicated in Figure 4.7 (c). When the droplets with identical volume have different anchoring strengths, the tactoid with large anchoring strength is elongated and the specific surface area becomes larger. If these droplets are composed of the same rod-like particles, the particles of elongated tactoid prefer to contact with the outer side of the droplet than the inside particles. The SWCNTs with large ζ potential repel each other, therefore, the tactoid has an elongated shape and acquires large anchoring strength. In addition, the previously reported value for SWCNT-CSA solution was $\omega = 5.6$ [41]. Because the repulsive force between protonated SWCNTs is higher than that of surfactant-stabilized SWCNTs, a larger ω may be obtained. On the other hand, in previous research on amyloid fibers, the anchoring strength decreased as the length of the mesogen decreased[48]. In this study, a clear relationship between the anchoring strength and the SWCNT aspect ratio was not observed. Therefore, it is assumed that the tactoid behaviors of SWCNT and amyloid fibers occurred for different causes.
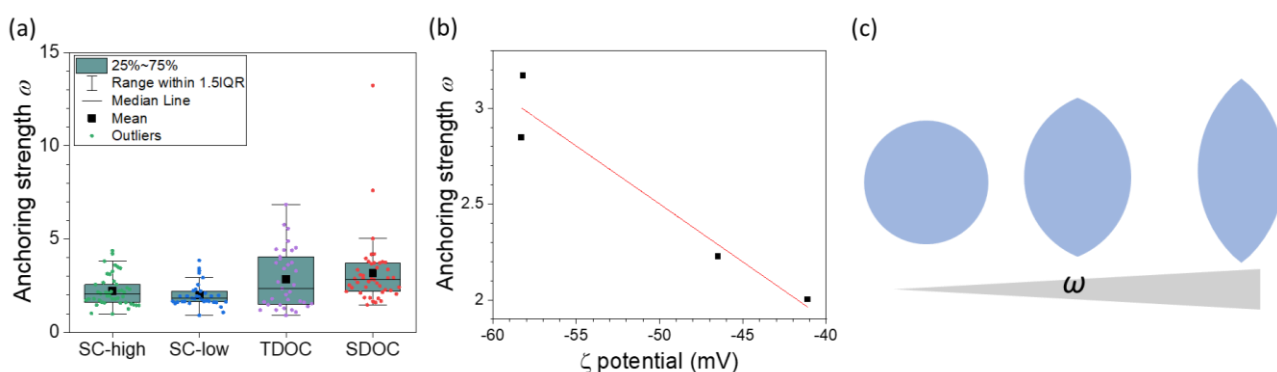

Figure 4.7 (a) A plot of the calculated anchoring strength of homogenous tactoid in each sample. (b) A plot of the anchoring strength against the ζ potentials. (c) Schematic of the droplets of identical volume with different anchoring strengths.

4.3.2　Schlieren textures in nematic phase of SC-low dispersion

Next, the arrangements of SWCNTs in the nematic LC phase were examined. Figures 4.8 and 4.9 show the polarized optical microscope images with a crossed Nicols configuration of the SC-low dispersion at a concentration of 0.49 vol%. A system of black stripes (the so-called Schlieren texture) was observed. The Schlieren texture exhibited distinct black brushes that emanated from singular points (disclinations) and were located in the regions where the director (or the local optical axis) was either parallel or orthogonal to the plane of polarization of the incident light. Generally, disclinations have four ($s = +1$ or -1) or two brushes ($s = +1/2$ or $-1/2$)[50]. In the present sample, only disclinations with two brushes ($s = \pm 1/2$) were observed.

The $\pm 1/2$ Schlieren texture can be distinguished by rotating the sample. Figure 4.8 (a) shows the POM images of a disclination with different sample angles, 0° - 330° in each 30°. The schematics of the brushes in Fig. 4.8 (a) were indicated in Fig. 4.8 (b). The rotation of brushes was counterclockwise as the sample rotated clockwise[50]. Figure 4.8 (c) shows the polarized microscope images of the 0-degree configuration with a tint plate inserted. Bluish and orangish colors indicate SWCNTs aligned parallel and orthogonal to the optical axis of the sensitive color plate, respectively. The SWCNTs were arranged as shown by the dotted lines in Fig. 4.8 (d). Therefore, the strength of this defect is assigned to $s = +1/2$.

The brush in Fig. 4.9 (a) rotated clockwise as the sample rotated clockwise (Schematics were indicated in Fig. 4.9 (b))[50]. Based on the images with the sensitive tint plate (Fig. 4.9 (c)), the alignments of SWCNTs were similar to the dotted lines in Fig. 4.9 (d). Thus, the strength of this defect is attributed $s = -1/2$.
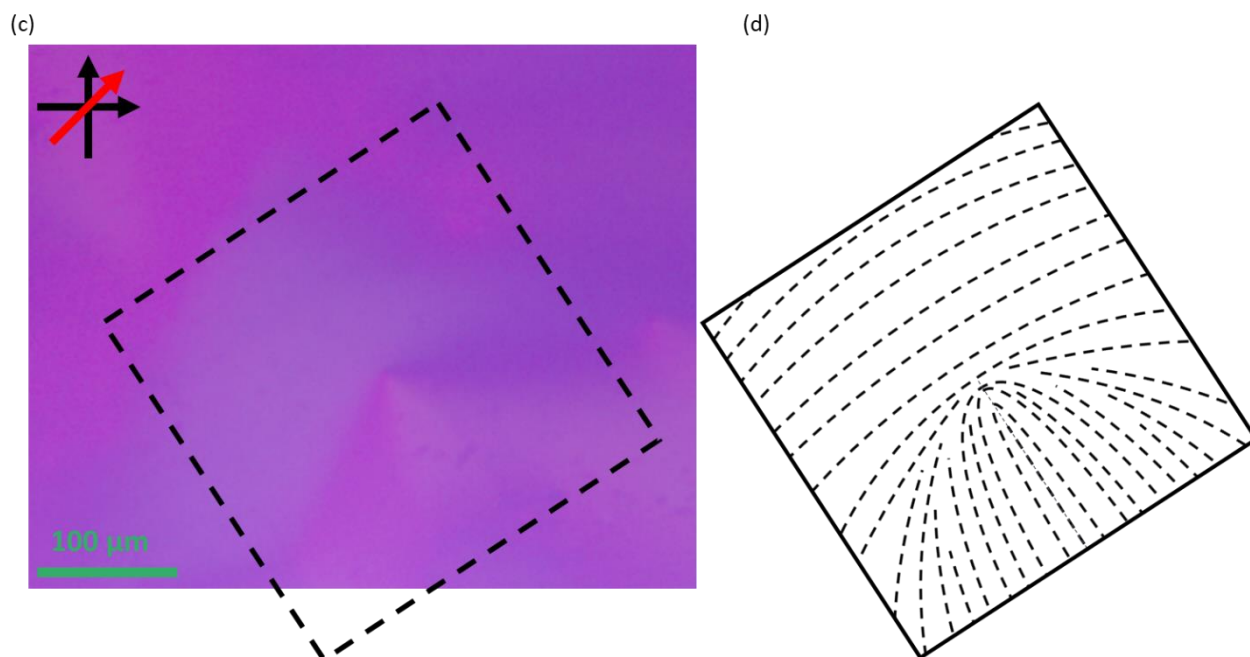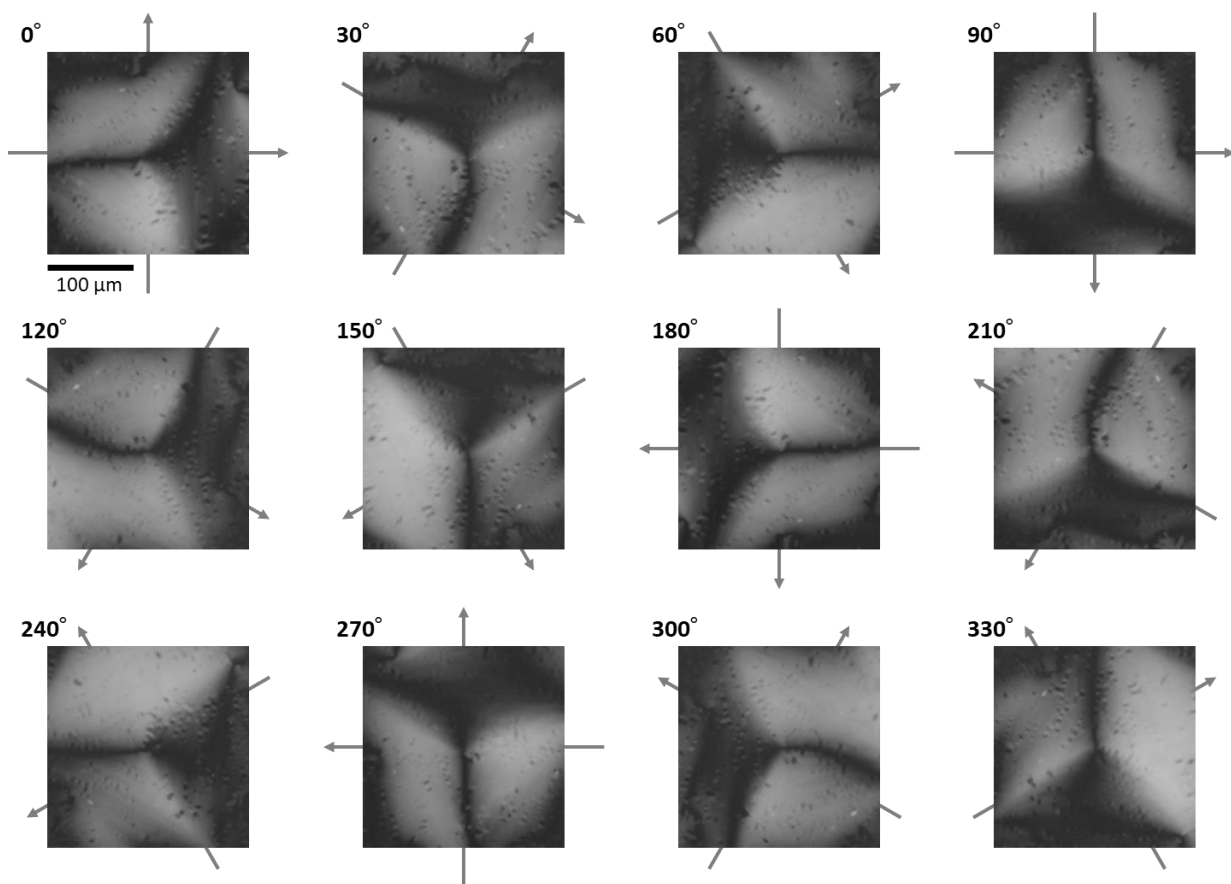
(c)

100 μm

(d)
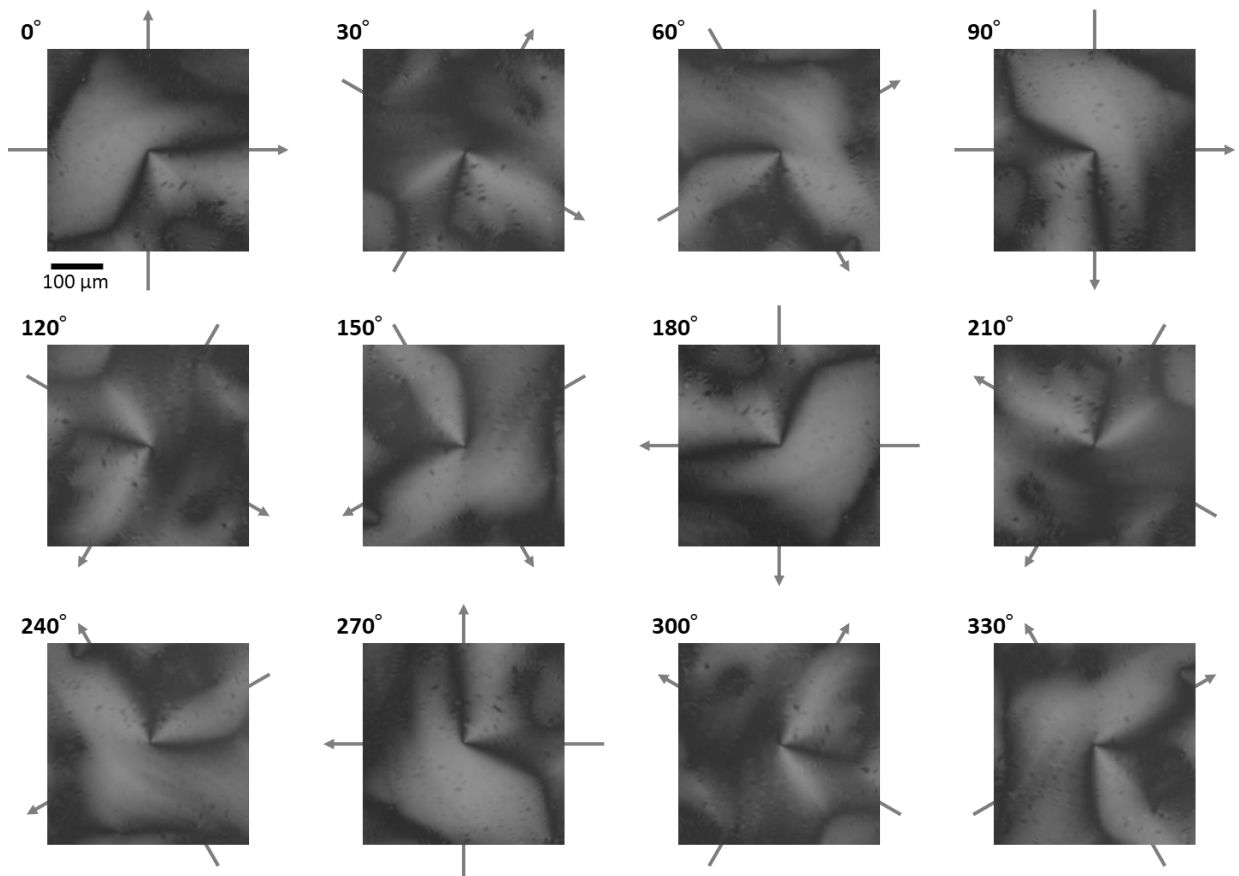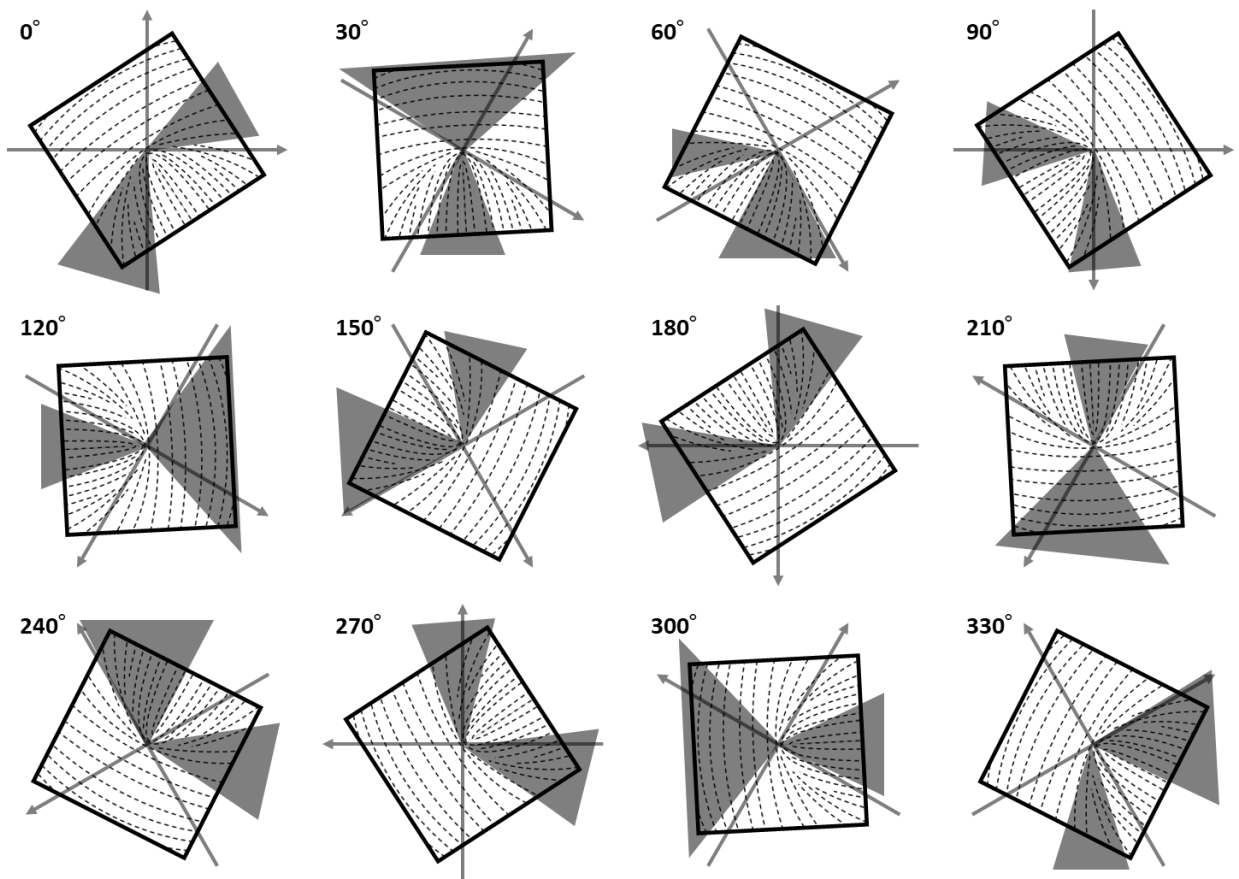
Figure 4.8 (a) POM images of the +1/2 schlieren structure with different sample angles, 0° - 330° in each 30°. (b) Schematics of the brushes observed in Fig. 4.8 (a). (c) POM image of the 0-degree configuration under crossed polarizers with a sensitive tint plate. Scale bar is 100 μm. Red arrow indicates the optical axis of the tint plate. (d) The corresponding schematic of SWCNT orientation in the enclosed part in Fig. 4.8 (c). (Reprinted with permission from K. Kojima *et al.*, *Langmuir* **2022**, *38*, 29, 8899–8905. Copyright 2022 American Chemical Society.)

(a)

0° 30° 60° 90°

100 μm

120° 150° 180° 210°

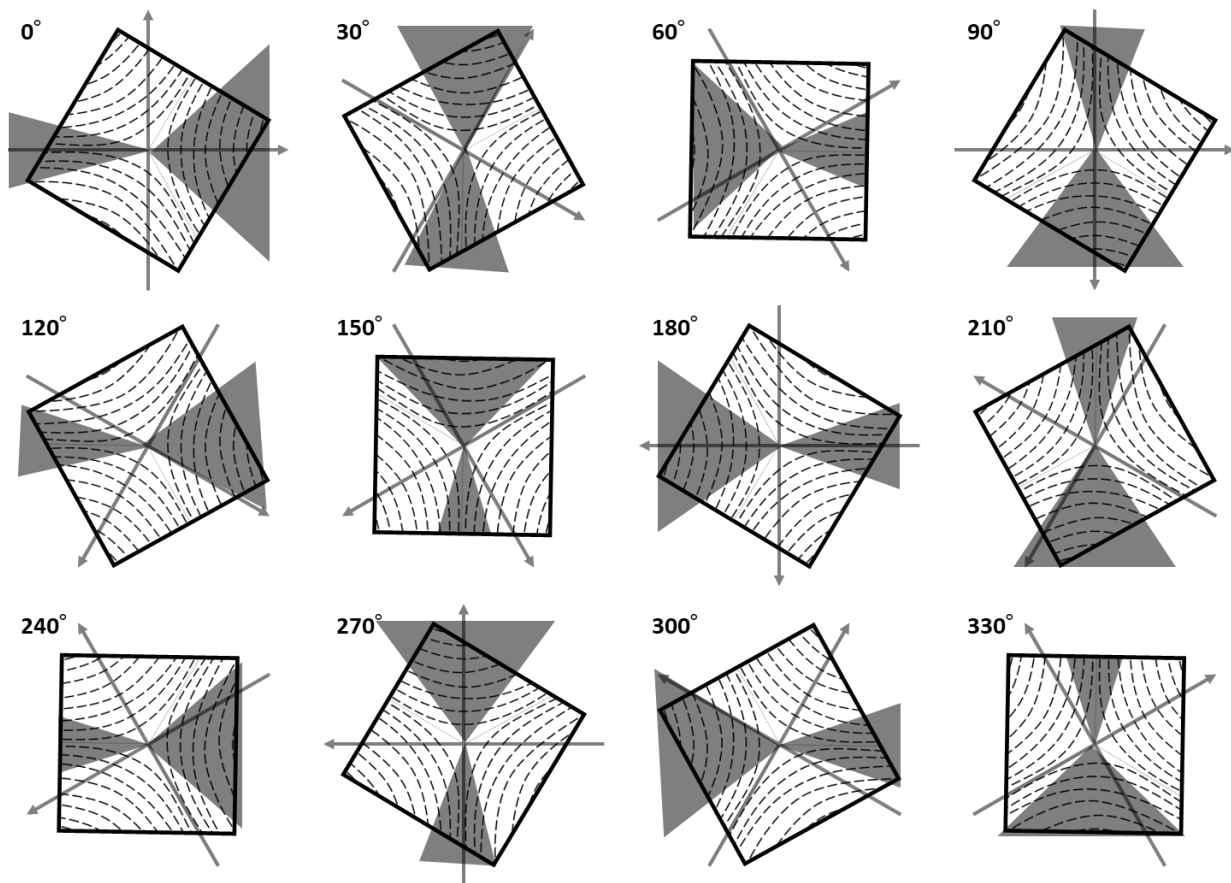240° 270° 300° 330°

(b)

0° 30° 60° 90°

120° 150° 180° 210°

240° 270° 300° 330°

Figure 4.9 (a) POM images of the -1/2 schlieren structure with different sample angles, 0° - 330° in each 30°. (b) Schematics of the brushes observed in Fig. 4.9 (a). (c) POM image of the 0-degree configuration under crossed polarizers with a sensitive tint plate. Scale bar is 100 μm. Red arrow indicates the optical axis of the tint plate. (d) The corresponding schematic of SWCNT orientation in the enclosed part in Fig. 4.9 (c). (Reprinted with permission from K. Kojima *et al.*, *Langmuir* **2022**, *38*, 29, 8899–8905. Copyright 2022 American Chemical Society.)
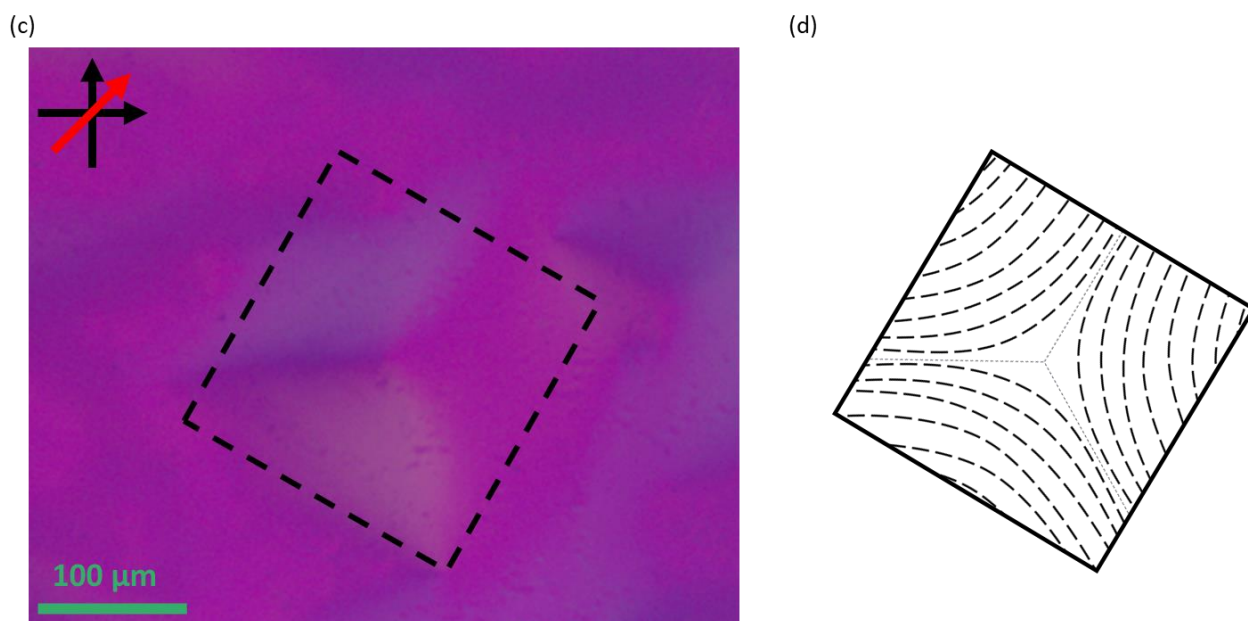
The positive or negative value of the strengths depends on the balance between the bend and splay distortions[51,52]. For instance, the Frank bend distortion is energetically favored for +1/2 defects, whereas the splay packing becomes more favorable in −1/2 defects. For the present sample, the number of $s = +1/2$ and the number of $s = −1/2$ were almost the same (Fig. 4.10), suggesting that the bend and splay elastic moduli of the SWCNT in SC-low dispersion were close to each other.
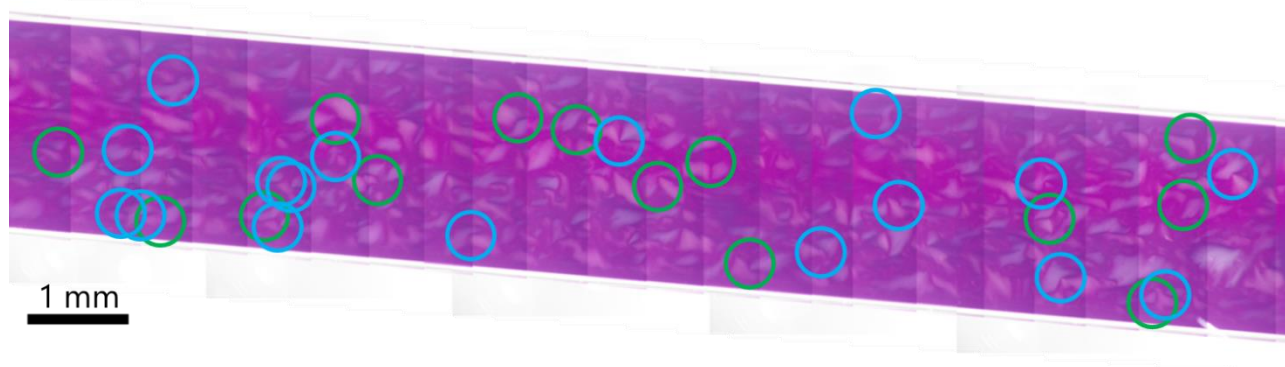

Figure 4.10 Polarized optical microscope image of the nematic phase (0.49 vol%). Blue and green circles correspond to $s = +1/2$ and $s = −1/2$ strength disclinations, respectively. (Reprinted with permission from K. Kojima *et al.*, *Langmuir* **2022**, *38*, 29, 8899–8905. Copyright 2022 American Chemical Society.)

4.4 Conclusion

The shapes of the spindle-shaped nematic LC, or the so-called tactoids, in the biphasic state were examined in detail. The homogenous and bipolar tactoid were observed in the biphasic state of all samples. The alignments of the SWCNTs in the tactoids were directly observed under a crossed Nicols polarized optical microscope with a sensitive tint plate. The homogenous tactoid changed to bipolar tactoid during tactoid volume growth. The transition volume of tactoids becomes larger along with larger SWCNT L/D. The relationship between the anchor strength of the tactoids and the ζ potentials was assumed, but further research is needed to support this hypothesis.

The Schlieren textures were successfully observed in the nematic phase of the SWCNT dispersion by POM with a tint plate inserted, which is the first experimental demonstration of the SWCNT alignment at the liquid phase. The disclinations with the strengths of $s = +1/2$ and $s = -1/2$ appeared at almost the same frequencies, indicating that the splay and the bend elastic modulus of the SWCNT bundles had almost identical values.

Chapter 5   Summary

  In this thesis, the phase transitions of liquid crystalline SWCNT dispersions were studied and LC phases of SWCNT were observed by POM in detail.

  Optimizing the dispersion process by optical microscopy and DCS analysis, the dispersions which contain rod-like SWCNTs as the main components were prepared. Using these optimized dispersions, phase transitions were observed with an increase in SWCNT concentration. The dispersion which shows the isotropic phase in low concentration was changed to the nematic phase via a biphasic state, in which the isotropic and nematic phases were coexisting. Comparing the dispersions with different SWCNT aspect ratios *L/D*, the phase transition concentration of high *L/D* SWCNT was lower than that of low *L/D* SWCNT. It denotes the same tendency as the Onsager theory (Chapter 2). Furthermore, comparing the dispersions with the aid of different surfactants, in which the aspect ratios of constituent SWCNTs were almost the same, the phase transition concentrations were slightly affected by the surface charge of rod-like SWCNTs. From the measurements of ζ potential, SWCNTs with large repulsive forces needed high concentration to phase transition (Chapter 3). In the nematic phases, all samples show full range birefringence, but the size of LC domains was different. The dispersion which contained SWCNTs with the largest diameter had the largest LC domains because the constituent SWCNTs had high rigidity. On the other hand, the SWCNT film with high order parameters was made from the dispersion which contained high *L/D* SWCNTs. The dispersion which contains SWCNTs with a higher aspect ratio is preferable to preparing highly ordered SWCNT materials.

  Furthermore, the SWCNT orientations in LC phases were estimated by POM with a tint plate inserted. The spindle-like nematic LC droplets, "tactoids", were observed in the biphasic states and classified into two groups, homogenous and bipolar, by constituted SWCNT orientations. The transition of tactoids from homogenous to bipolar occurred with the volume growth of tactoids, and the transition volume related to the aspect ratio of constituent SWCNTs. Additionally, in the nematic phase with large LC domains, the $\pm 1/2$ Schlieren textures were observed. It is the first time that the SWCNT orientations of the Schlieren textures in the liquid phase were observed (Chapter 4).

  The results of this thesis provide guidelines for preparing liquid crystalline surfactant-stabilized SWCNT dispersions. Since superior properties of SWCNT, such as electrical conductivity, appear along the tube direction, the methods of controlling SWCNT orientation are extremely important to manufacture high-performance SWCNT materials. Because the liquid crystalline SWCNT dispersions are considered raw materials to prepare highly ordered SWCNT materials, the improvement of SWCNT orientation in materials is expected by producing liquid crystalline SWCNT dispersions based on this thesis.

List of references

1) S. Iijima and T. Ichihashi, "Single-shell carbon nanotubes of 1-nm diameter", *Nature* **1993**, *363*, 603-605.

2) M.S. Dresselhaus, G. Dresselhaus, P. Avouris, Eds. *Carbon Nanotubes: Synthesis, Structure, Properties, and Applications (Topics in Applied Physics 80)*; Springer-Verlag: Berlin, 2001.

3) A. Jorio, G. Dresselhaus, M.S. Dresselhaus, Eds. *Carbon Nanotubes: Advanced Topics in the Synthesis, Structure, Properties and Applications (Topics in Applied Physics 111)*; Springer-Verlag: Berlin, 2008.

4) L. Qian, Y. Xie, M. Zou, and J. Zhang, *J. Am. Chem. Soc.* **2021**, *143*, 45, 18805-18819.

5) P. Sehrawat, C. Julien, S.S. Islam, "Carbon nanotubes in Li-ion batteries: A review", *Materials Science and Engineering: B* **2016**, *213*, 12-40.

6) National Institute of Advanced Industrial Science and Technology (2020, February 13), *Long lifetime and heat/pressure resistant O-ring developed at AIST goes on sale* [Press release]. https://www.aist.go.jp/aist_e/list/latest_research/2020/20200213/en20200213.html

7) H. Jintoku and Y. Matsuzawa, "Carbon nanotube liquid crystal dispersion for large-area, micropatterned aligned films", *ACS Appl. Nano Mater.* **2022**, *5*, 2, 2195-2203.

8) N. Tajima, T. Watanabe, T. Morimoto, K. Kobashi, K. Mukai, K. Asaka, and T. Okazaki, "Nanotube length and density dependences of electrical and mechanical properties of carbon nanotube fibres made by wet spinning", *Carbon* **2019**, *152*, 1-6.

9) T. Watanabe, S. Yamazaki, S. Yamashita, T. Inaba, S. Muroga, T. Morimoto, K. Kobashi, and T. Okazaki, "Comprehensive characterization of structural, electrical, and mechanical properties of carbon nanotube yarns produced by various spinning methods", *Nanomaterials* **2022**, *12*(4), 593.

10) B. Natarajan, "Processing-structure-mechanical property relationships in direct formed carbon nanotube articles and their composites: A review", *Composites Science and Technology* **2022**, *225*, 109501.

11) M. Zhang, K.R. Atkinson, and R.H. Baughman, "Multifunctional carbon nanotube yarns by downsizing an ancient technology", *Science* **2004**, *306*, 5700, 1358-1361.

12) V.T. Dau, D.V. Dao, T. Yamada, B.T. Tung, K. Hata, and S. Sugiyama, "Integration of SWCNT film into MEMS for a micro-thermoelectric device", *Smart Mater. Struct.* **2010**, *19*, 075003.

13) Y. Li, I.A. Kinloch, and A.H. Windle, "Direct spinning of carbon nanotube fibers from chemical vapor deposition synthesis", *Science* **2004**, *304*, 5668, 276-278.

14) N. Behabtu, C.C. Young, D.E. Tsentalovich, O. Kleinerman, X. Wang, A.W.K. Ma, E.A. Bengio, R.F. Ter Waarbeek, J.J. De Jong, R.E. Hoogerwerf, S.B. Fairchild, J.B. Ferguson, B. Maruyama, J. Kono, Y. Talmon, Y. Cohen, M.J. Otto, and M. Pasquali, "Strong, light, multifunctional fibers of carbon nanotubes with ultrahigh conductivity", *Science* **2013**, *339*, 6116, 182-186.

15) R.J. Headrick, D.E. Tsentalovich, J. Berdegue, E.A. Bengio, L. Liberman, O. Kleinerman, M.S. Lucas, Y. Talmon, and M. Pasquali, "Structure-property relations in carbon nanotube fibers by downscaling solution processing", *Adv. Mater.* **2018**, *30*, 9, 1704482.

16) V.A. Davis, L.M. Ericson, A.N.G. Parra-Vasquez, H. Fan, Y. Wang, V. Prieto, J.A. Longoria, S. Ramesh, R.K. Saini, C. Kittrell, W.E. Billups, W.W. Adams, R.H. Hauge, R.E. Smalley, and M. Pasquali, "Phase behavior and rheology of SWCNTs in superacids", *Macromolecules* **2004**, *37*, 1, 154-160.

17) S. Ramesh, L.M. Ericson, V.A. Davis, R.K. Saini, C. Kittrell, M. Pasquali, W.E. Billups, W.W. Adams, R.H. Hauge, and R.E. Smalley, "Dissolution of pristine single walled carbon nanotubes in superacids by direct protonation", *J. Phys. Chem. B* **2004**, *108*, 26, 8794-8798.

18) S. Badaire, C. Zakri, M. Maugey, A. Derre, J.N. Barisci, G. Wallace, and P. Poulin, "Liquid crystals of DNA-stabilized carbon nanotubes", *Adv. Mater.* **2005**, *17*, 1673-1676.

19) P.K. Rai, R.A. Pinnick, A.N.G. Parra-Vasquez, V.A. Davis, H.K. Schmidt, R.H. Hauge, R.E. Smalley, and M. Pasquali, "Isotropic−nematic phase transition of single-walled carbon nanotubes in strong acids", *J. Am. Chem. Soc.* **2006**, *128*, 2, 591-595.

20) S.E. Moulton, M. Maugey, P. Poulin, and G.G. Wallace, "Liquid crystal behavior of single-walled carbon nanotubes dispersed in biological hyaluronic acid solutions", *J. Am. Chem. Soc.* **2007**, *129*, 30, 9452-9457.

21) V.A. Davis, A.N.G. Parra-Vasquez, M.J. Green, P.K. Rai, N. Behabtu, V. Prieto, R.D. Booker, J. Schmidt, E. Kesselman, W. Zhou, H. Fan, W.W. Adams, R.H. Hauge, J.E. Fischer, Y. Cohen, Y. Talmon, R.E. Smalley, and M. Pasquali, "True solutions of single-walled carbon nanotubes for assembly into macroscopic materials", *Nature Nanotechnology* **2009**, *4*, 830-834.

22) L. Lu and W. Chen, "Large-scale aligned carbon nanotubes from their purified, highly concentrated suspension", *ACS Nano* **2010**, *4*, 2, 1042-1048.

23) S. Zhang, Q. Li, I.A. Kinloch, and A.H. Windle, "Ordering in a droplet of an aqueous suspension of single-wall carbon nanotubes on a solid substrate", *Langmuir* **2010**, *26*, 3, 2107-2112.

24) N. Puech, C. Blanc, E. Grelet, C. Zamora-Ledezma, M. Maugey, C. Zakri, E. Anglaret, and P. Poulin, "Highly ordered carbon nanotube nematic liquid crystals", *J. Phys. Chem. C* **2011**, *115*, 8, 3272-3278.

25) G. Ao, D. Nepal, M. Aono, and V.A. Davis, "Cholesteric and nematic liquid crystalline phase behavior of double-stranded DNA stabilized single-walled carbon nanotube dispersions", *ACS Nano* **2011**, *5*, 2, 1450-1458.

26) F. Tardani, C.L. Mesa, P. Poulin, and M. Maugey, "Phase behavior of DNA-based dispersions containing carbon nanotubes: Effects of added polymers and ionic strength on excluded volume", *J. Phys. Chem. C* **2012**, *116*, 18, 9888-9894.

27) C. Zakri, C. Blanc, E. Grelet, C. Zamora-Ledezma, N. Puech, E. Anglaret, and P. Poulin, "Liquid crystals of carbon nanotubes and graphene", *Philos. Trans. R. Soc. A* **2013**, *371*, 1988, 20120499 (2013).

28) L. Maillaud, R.J. Headrick, V. Jamali, J. Mailaud, D.E. Tsentalovich, W. Neri, E.A. Bengio, F. Mirri, O. Kleinerman, Y. Talmon, P. Poulin, and M. Pasquali, "Highly concentrated aqueous dispersions of carbon nanotubes for flexible and conductive fibers", *Ind. Eng. Chem. Res.* **2018**, *57*, 10, 3554-3560.

29) P. Wang, B. Barnes, X. Wu, H. Qu, C. Zhang, Y. Shi, R.J. Headrick, M. Pasquali, and Y. H. Wang, "Self-sorting of 10-μm-long single-walled carbon nanotubes in aqueous solution", *Adv. Mater.* **2019**, *31*, 1901641.

30) R.J. Headrick, S.M. Williams, C.E. Owens, L.W. Taylor, O.S. Dewey, C.J. Ginestra, L. Liberman, A.M. Ya'akobi, Y. Talmon, B. Maruyama, G.H. Mckinley, A. John Hart, and M. Pasquali, "Versatile acid solvents for pristine carbon nanotube assembly", *Sci. Adv.* **2022**, *8*, 17, eabm3285.

31) Y. Kato, T. Morimoto, K. Kobashi, T. Yamada, T. Okazaki, and K. Hata, "Quantitative method for analyzing dendritic carbon nanotube agglomerates in dispersions using differential centrifugal sedimentation", *J. Phys. Chem. C* **2019**, *123*, 34, 21252-21256.

32) A.R. Henn, "Calculation of the Stokes and aerodynamic equivalent diameters of a short reinforcing fiber", *Part. Part. Syst. Charact.* **1996**, *13*, 249-253.

33) K. Kobashi, A. Sekiguchi, T. Yamada, S. Muroga, and T. Okazaki, "Dispersions of high-quality carbon nanotubes with narrow aggregate size distributions by viscous liquid for conducting polymer composites", *ACS Appl. Nano Mater.* **2020**, *3*, 2, 1391-1399.

34) K. Kobashi, S. Ata, T. Yamada, D.N. Futaba, T. Okazaki, and K. Hata, "Classification of commercialized carbon nanotubes into three general categories as a guide for applications", *ACS Appl. Nano. Mater.* **2019**, *2*, 7, 4043-4047.

35) L. Shi, P. Rohringer, P. Ayala, T. Saito, and T. Pichler, "Carbon nanotubes from enhanced direct injection pyrolytic synthesis as templates for long linear carbon chain formation", *Phys. Status Solidi B* **2013**, *250*, 12, 2611-2615.

36) K. Hata, D.N. Futaba, K. Mizuno, T. Namai, M. Yumura, and S. Iijima, "Water-assisted highly efficient synthesis of impurity-free single-walled carbon nanotubes", *Science* **2004**, *306*, 5700, 1362-1364.

37) B. Kitiyanan, W.E. Alvarez, J.H. Harwell, and D.E. Resasco, "Controlled production of single-wall carbon nanotubes by catalytic decomposition of CO on bimetallic Co–Mo catalysts", *Chemical Physics Letters* **2000**, *317*, 3-5, 497-503.

38) S. Okubo, T. Okazaki, N. Kishi, S. Joung, T. Nakanishi, S. Okada, and S. Iijima, "Diameter-dependent band gap modification of single-walled carbon nanotubes by encapsulated fullerenes", *J. Phys. Chem. C* **2009**, *113*, 571-575.

39) P. Prinsen and P. van der Schoot, "Shape and director-field transformation of tactoids", *Phys. Rev. E* **2003**, *68*, 021701.

40) N. Puech, E. Grelet, P. Poulin, C. Blanc, and P. van der Schoot, "Nematic droplets in aqueous dispersions of carbon nanotubes", *Phys. Rev. E* **2010**, *82*, 020702(R).

41) V. Jamali, N. Behabtu, B. Senyuk, J.A. Lee, I.I. Smalyukh, P. van der Schoot, and M. Pasquali, "Experimental realization of crossover in shape and director field of nematic tactoids", *Phys. Rev. E* **2015**, *91*, 042507.

42) L. Onsager, "The effects of shape on the interaction of colloidal particles", *Ann. N.Y. Acad. Sci.* **1949**, *51*, 627.

43) M.J. Green, A.N.G. Parra-Vasquez, N. Behabtu, and M. Pasquali, "Modeling the phase behavior of polydisperse rigid rods with attractive interactions with applications to single-walled carbon nanotubes in superacids", *J. Chem. Phys.* **2009**, *131*, 084901.

44) W. Song and A.H. Windle, "Size-dependence and elasticity of liquid-crystalline multiwalled carbon nanotubes", *Adv. Mater.* **2008**, *20*, 16, 3149-3154.

45) A. Babaei-Ghazvini and B. Achaya, "Influence of cellulose nanocrystal aspect ratio on shear force aligned films: Physical and mechanical properties", *Carbohydrate Polym. Technol. Appl.* **2022**, *3*, 100217.

46) A. Babaei-Ghazvini, B. Achaya, and D.R. Korber, "Multilayer photonic films based on interlocked chiral-nematic cellulose nanocrystals in starch/chitosan", *Carbohydrate Polym.* **2022**, *275*, 118709.

47) X. Wu, K. Mukai, K. Asaka, T. Morimoto, and T. Okazaki, "Effect of surfactants and dispersion methods on properties of single-walled carbon nanotube fibers formed by wet-spinning", *Appl. Phys. Express* **2017**, *10*, 055101.

48) M. Bagnani, G. Nystrom, C. De Michele, and R. Mezzenga, "Amyloid fibrils length controls shape and structure of nematic and cholesteric tactoids", *ACS Nano* **2019**, *13*, 591-600.

49) H. Awaya, *Koubunshisozai no Henkoukenbikyou Nyuumon (Isagoge of polarized optical microscope for polymers)*; AGNE Gijutsu Center Inc.: Tokyo, 2001, p.77.

50) Demus, D.; Richter, R. *Textures of Liquid Crystals*; Verlag Chemie: Weinheim, 1978.

51) C. Chang, L. Lu, J. Liu, and W. Chen, "Bending deformation mechanism and defective properties of liquid crystalline carbon nanotubes in evaporating droplets", *RSC Adv.* **2011**, *1*, 3, 468-473.

52) C. Chang, Y. Zhao, Y. Liu, and L. An, "Liquid crystallinity of carbon nanotubes", *RSC Adv.* **2018**, *8*, 28, 15780-15795.

List of achievements

Publications

1. <u>K. Kojima</u>, H. Jintoku, Y. Kuwahara, M. Aizawa, T. Yamamoto, S. Muroga, K. Kobashi, and T. Okazaki, "Liquid-crystalline behaviors of single-walled carbon nanotube aqueous dispersions with different nanotube aspect ratios and surfactants", *Applied Physics Express* **2022**, *15*, 125003. (Chapter 2, 3, 4)

2. <u>K. Kojima</u>, M. Aizawa, T. Yamamoto, S. Muroga, K. Kobashi, and T. Okazaki, "Liquid crystalline behaviors of single-walled carbon nanotubes in an aqueous sodium cholate dispersion", *Langmuir* **2022**, *38*, 29, 8899-8905. (Chapter 2, 4)

Oral presentation

1. ○<u>K. Kojima</u>, M. Aizawa, T. Yamamoto, K. Kobashi, T. Okazaki, "Preparation and Characterization of Carbon Nanotube Dispersion Exhibiting Liquid Crystal Phase", The 102nd CSJ Annual Meeting (2022), 2022.03.

Poster presentations

1. ○<u>K. Kojima</u>, M. Aizawa, T. Yamamoto, S. Muroga, K. Kobashi, T. Okazaki, "Liquid crystalline behaviors of single-walled carbon nanotubes in aqueous sodium cholate dispersions", The 63rd Fullerenes-Nanotubes-Graphene General Symposium, 2022.09.

Award

1. Young Scientist Poster Award, The 63rd Fullerenes-Nanotubes-Graphene General Symposium (2022, September 1)

Acknowledgement